



HAL
open science

Inferring the dust emission at submillimeter and millimeter wavelengths using neural networks

D. Paradis, C. Mény, A. Noriega-Crespo, K. Demyk, I. Ristorcelli, Nathalie Ysard

► **To cite this version:**

D. Paradis, C. Mény, A. Noriega-Crespo, K. Demyk, I. Ristorcelli, et al.. Inferring the dust emission at submillimeter and millimeter wavelengths using neural networks. *Astronomy and Astrophysics - A&A*, 2024, 691, pp.A241. 10.1051/0004-6361/202451422 . hal-04774233

HAL Id: hal-04774233

<https://hal.science/hal-04774233v1>

Submitted on 26 Nov 2024

HAL is a multi-disciplinary open access archive for the deposit and dissemination of scientific research documents, whether they are published or not. The documents may come from teaching and research institutions in France or abroad, or from public or private research centers.

L'archive ouverte pluridisciplinaire **HAL**, est destinée au dépôt et à la diffusion de documents scientifiques de niveau recherche, publiés ou non, émanant des établissements d'enseignement et de recherche français ou étrangers, des laboratoires publics ou privés.

Inferring the dust emission at submillimeter and millimeter wavelengths using neural networks

D. Paradis^{1,*}, C. Mény¹, A. Noriega-Crespo², K. Demyk¹, I. Ristorcelli¹, and N. Ysard^{1,3}

¹ IRAP, Université de Toulouse, CNRS, UPS, 9 Av. du Colonel Roche, BP 44346, 31028 Toulouse, cedex 4, France

² Space Telescope Science Institute, 3700 San Martin Drive, Baltimore, MD 21218, USA

³ Université Paris-Saclay, CNRS, Institut d'Astrophysique Spatiale, 91405 Orsay, France

Received 8 July 2024 / Accepted 15 September 2024

ABSTRACT

Context. The *Planck* mission provided all-sky dust emission maps in the submillimeter (submm) to millimeter (mm) range at an angular resolution of $5'$. In addition, some specific sources can be observed at long wavelengths and higher resolution using ground-based telescopes. These observations are limited to small scales and are sometimes not delivered to the community. These ground-based observations require extensive data processing before they become available for scientific analysis, and suffer from extended emission filtering.

Aims. At present, we are still unable to fully understand the emissivity variations observed in different astrophysical environments at long (submm and mm) wavelengths. Several models have been developed to reproduce the diffuse Galactic medium, and each distinct environment requires an adjustment of the models. It is therefore challenging to estimate any dust emission in the submm-mm at a better resolution than the $5'$ from *Planck*. In this analysis, based on supervised deep learning algorithms, we produced dust emission predictions in the two *Planck* bands centered at $850\ \mu\text{m}$ (353 GHz) and $1.38\ \text{mm}$ (217 GHz) at the *Herschel* resolution ($37''$). Prediction or forecasting is a frequently used term in machine learning or neural network research that refers to the output of an algorithm that has been trained on a given dataset and that is being used for modeling purposes.

Methods. *Herschel* data of Galactic environments, ranging from $160\ \mu\text{m}$ to $500\ \mu\text{m}$ and smoothed to an angular resolution of $5'$, were used to train the neural network. This training aimed to provide the most accurate model for reproducing *Planck* maps of dust emission at $850\ \mu\text{m}$ and $1.38\ \text{mm}$. Then, using *Herschel* data only, the model was applied to predict dust emission maps at $37''$.

Results. The neural network is capable of reproducing dust emission maps of various Galactic environments with a difference of only a few percent at the *Planck* resolution. Remarkably, it also performs well for nearby extragalactic environments. This could indicate that large dust grains, probed by submm or mm observations, have similar properties in both our Galaxy and nearby galaxies, or at least that their spectral behaviors are comparable in Galactic and extragalactic environments. For the first time, we provide to the community dust emission prediction maps at $850\ \mu\text{m}$ and $1.38\ \text{mm}$ at the $37''$ of several surveys: Hi-GAL, Gould Belt, Cold Cores, HERITAGE, Helga, HerM33es, KINGFISH, and Very Nearby Galaxies. The ratio of these two wavelength brightness bands reveals a derived emissivity spectral index statistically close to 1 for all the surveys, which favors the hypothesis of a flattened dust emission spectrum for wavelengths larger than $850\ \mu\text{m}$.

Conclusions. Neural networks appear to be powerful algorithms that are highly efficient at learning from large datasets and achieving accurate reproductions with a deviation of only a few percent. However, to fully recover the input data during the training, it is essential to sample a sufficiently large range of datasets and physical conditions.

Key words. dust, extinction – infrared: ISM – submillimeter: ISM

1. Introduction

Reproducing the global spectral behavior of dust emission throughout our Galaxy from the infrared (IR) to the millimeter (mm) with dust models has proven to be more difficult than envisioned. In this wavelength regime, the sky brightness ($I_\nu(\lambda)$) is often simply described by a single modified black-body model, assuming a single dust temperature (T) and spectral index (β) along the line of sight and an optically thin medium. Even in the diffuse interstellar medium (ISM) of our Galaxy, where the largest grains may be thought to be at a single temperature and to have homogeneous properties, there is no consensus yet on either the dust temperature determination or the exact spectral shape of the dust emission in the far-infrared (FIR) to mm. The sub-millimeter (submm) behavior varies over the sky and its variations are not yet understood. This behavior could be the result of a nonuniformity in the emissivity power law through the environments – in other words, β variations – or the result

of a break in the emissivity power law described by a change in β from the FIR to the submm (usually described as a two modified black-body model). The spectral behavior of the emissivity is not constant over the sky and the origin of these variations is still uncertain. Several dust emission models have been developed in order to reproduce the emission of the large-scale diffuse ISM in our Galaxy (Désert et al. 1990; Draine and Li 2007; Compiègne et al. 2011; Jones et al. 2013; Siebenmorgen 2023; Hensley and Draine 2023; Ysard et al. 2024). Unfortunately, the interpretation of the dust emission spectrum relies on the dust model being used. At present, large-scale observations at long wavelengths ($>500\ \mu\text{m}$) only exist at an angular resolution of $5'$, thanks to the *Planck*¹ mission (Planck Collaboration I 2011).

¹ *Planck* (<http://www.esa.int/Planck>) is a project of the European Space Agency – ESA – with instruments provided by two scientific consortia funded by ESA member states (in particular the lead countries: France and Italy) with contributions from NASA (USA), and telescope reflectors provided in a collaboration between ESA and a scientific Consortium led and funded by Denmark.

* Corresponding author; deborah.paradis@irap.omp.eu

It is therefore not possible to investigate from large surveys the dust emission at small scales in this wavelength range. Ground-based observatories from facilities such as ALMA and NOEMA, or instruments such as SCUBA-2, Bolocam, and NIKA2, can provide continuum observations of dust at high angular resolution for specific sources at long wavelengths (see for instance Sadavoy et al. 2013; Enoch et al. 2006; Turner et al. 2019; Katsioli et al. 2023). However, some of the observations are not available to the community. In addition, the reduction of the data is a complex task and most of the extended emission is lost when removing the contribution from Earth’s atmosphere. Furthermore, to properly compare these observations with those of space-based telescopes, a specific filtering should be applied to the on-board satellite observations. Only a few experts are able to properly perform this kind of processing (Roussel et al. 2020, for example).

The submm and mm wavelength data are crucial to explore the behavior of the dust emission spectrum. Using *Herschel*² data, Juvela et al. (2015) evidenced statistically an increase in the dust spectral index toward the coldest regions of Galactic cold cores. They obtained values significantly larger than the mean value of ~ 1.6 obtained for the diffuse Galactic emission (Planck Collaboration XI 2020). Paradis et al. (2014) also showed distinct trends in the dust emission between cold and warm Galactic environments, with changes in the dust emissivity index, using *Herschel* data. Several studies have also revealed variations in the spectral index over large areas (see for instance Paradis et al. 2012b; Planck Collaboration Int. XXIX 2016). Variations in β across the high-latitude sky between $\beta = 1$ and $\beta = 2$ with a $30'$ angular resolution have been reported, along with an optical depth different than the one expected from uniform dust emission properties. Grain coagulation from the diffuse to the dense medium could explain the relative change in the dust emission behavior between these two environments. Indeed, grain coagulation is expected in cold regions due to the presence of ice mantle at the surface of the grains (Stepnik et al. 2003; Kohler et al. 2011, 2012; Jones et al. 2013; Ysard et al. 2015) and could engender a change in the emissivity spectral shape. The two-level-system model (Mény et al. 2007; Paradis et al. 2011), which takes the physical aspect of amorphous dust material into account, could also explain the emissivity behavior. Indeed, dust in the ISM is mostly amorphous, as is evidenced by the $10\ \mu\text{m}$ silicate absorption profile in the region around Sgr A* (Kemper et al. 2004). The dust injected in the ISM after its formation in AGB stars is amorphous and crystalline in proportions that are not known. The absence of crystalline dust in the ISM probably results from the processing of the dust grain by cosmic rays and supernovae-generated shock waves.

Draine & Hensley (2012) argues that the flattening of the dust emission spectrum could be partly explained by a mixture of normal dust with a population of small magnetic nano-particles, such as metallic iron, magnetite Fe_3O_4 , or maghemite $\gamma\text{-Fe}_2\text{O}_3$. However, the addition of spinning dust is required to account for the observed spectral energy distribution (SED) of the Small Magellanic Cloud (SMC) in the mm domain. Nevertheless, the results of Planck Collaboration XI (2020) using polarization data from *Planck* do not favor this hypothesis.

The resolution and sensitivity of *Herschel* data allowed the analysis of the ISM of more distant, but still close galaxies.

Dale et al. (2012) analyzed 61 nearby galaxies as part of the KINGFISH program, and found that the low-metallicity galaxies in the sample are not colder than average but reveal an excess of emission at $500\ \mu\text{m}$ with respect to the Draine & Li (2007) model fits. Even if this behavior is often detected in low-metallicity galaxies (Izotov et al. 2014) and the most significant excesses are detected in this type of environment (Galametz et al. 2011; Kirkpatrick et al. 2013; Rémy-Ruyer et al. 2013), the link between the excess and metallicity has not been demonstrated yet. Long-wavelength observations are crucial to explore the dust emission behavior. The *Planck* satellite has been precious to get dust emission information at long wavelengths, all over the sky. However, the combination of *Herschel* and *Planck* data induces a loss of resolution in the *Herschel* data. In that case, the SEDs of dust emission in external Galaxies are reduced to the global brightness in the galaxies and do not allow one to probe the ISM therein (see for instance Hermelo et al. 2016; Davies et al. 2017; Tibbs et al. 2018).

The outline of this paper is to produce dust prediction maps in the two *Planck* bands centered at $850\ \mu\text{m}$ (353 GHz) and $1.38\ \text{mm}$ (217 GHz) at the *Herschel* resolution ($37''$). Such maps could help us to understand the dust emission spectrum variations, to carefully derive dust masses in various environments, to help select targets to be observed at higher angular resolutions, or to undertake foreground subtraction. The content of the paper is as follows. After a brief description of the datasets, we explore the different correlations between multiwavelength data (Sect. 3). Then, we describe the neural network methodology in Sect. 4, and present different tools used in this analysis for manipulating HEALPix data (Sect. 5). In Sect. 6 we present the prediction maps we produced, in Sect. 7 we discuss some interesting results, and in Sect. 8 we summarize this work.

2. Data

2.1. Planck and additional components

We used the *Planck*/HFI $850\ \mu\text{m}$ and $1.38\ \text{mm}$ maps at an angular resolution of $5'$ (Planck Collaboration I 2011), corrected from the Zodiacal emission, available in the ESA archive³, to trace the dust emission. We used the *Planck* third release maps. Units in K_{CMB} have been converted to MJy/sr accordingly to Planck Collaboration IX (2014). We subtracted the cosmic infrared background (CIB) monopole prediction by removing $0.13\ \text{MJy/sr}$ and $0.033\ \text{MJy/sr}$ at $850\ \mu\text{m}$ and $1.38\ \text{mm}$, as is described in Planck Collaboration VIII (2014). We removed the CMB contribution in each HFI map by using the *Planck* CMB map reconstruction at $5'$ obtained from LGCMA⁴, a component separation method. As is evidenced in Planck Collaboration XIII (2014), a total of nine lines could contaminate the HFI channels. However, the authors concluded that only the $J = 1-0$, $J = 2-1$ and $J = 3-2$ CO lines could contribute to the total emission, with significant transitions at $100\ \text{GHz}$ ($3\ \text{mm}$) (50% of the total emission in molecular clouds and in the Galactic plane) and $217\ \text{GHz}$ ($1.38\ \text{mm}$) (15% of the total emission), weak at $353\ \text{GHz}$ ($850\ \mu\text{m}$) (less than 1%), respectively. Hence, the CO contamination is negligible in the other bands. The $217\ \text{GHz}$ data and $353\ \text{GHz}$ were corrected for CO contamination using the 12CO ($J = 2-1$) map produced as part of the Commander

² *Herschel* is an ESA space observatory with science instruments provided by European-led Principal Investigator consortia and with important participation from NASA.

³ <https://pla.esac.esa.int/>

⁴ see <http://www.cosmostat.org/product/>

multicomponent processing (Planck Collaboration X 2016). Following Planck Collaboration X (2016), free-free emission has a low impact at 217 GHz. Katsioli et al. (2023) decomposed the emission of the nearby edge-on galaxy NGC 891 at an angular resolution of 25'' into dust, free-free, and synchrotron emission from 1 mm to 20 cm. They found negligible free-free emission at 1.15 mm (less than 2%). The resulting *Planck* maps therefore represent the most reasonable description of the dust emission only. These are the final maps we use in the following.

2.2. *Herschel*

Thanks to the ‘‘Centre d’Analyse de Donnees Etendues’’ (CADE⁵), large maps of dust emission at different wavelengths and resolution, in the HEALPix format⁶, are available. For instance, the service delivers *Herschel* maps of the different large programs at 37'' (NSIDE = 16 384), 1' (NSIDE = 8192), and 4' (NSIDE = 2048) angular resolutions, all of which we have produced and made available on CADE. All *Herschel* data from this analysis come from this service. We used HEALPix maps from 70 μm to 500 μm of the Hi-GAL (Molinari et al. 2010), Galactic Cold Cores (Juvela et al. 2010), and Gould Belt (Andre et al. 2010) programs for training and testing the neural network. We added maps of the HERITAGE (Meixner et al. 2010), KINGFISH (Kennicutt et al. 2011), Very Nearby Galaxies (Bendo et al. 2012), HerM33es (Kramer et al. 2010), and Helga (Fritz et al. 2012) programs to predict dust emission maps. We used data at a 37'' angular resolution to predict dust emission, and 4' angular resolutions convolved to 5' to match the *Planck* resolution in order to train and test the neural network. With full HEALPix files, which is the case for the 4' files, the smoothing was performed using the *smoothing* function of the *healpy* Python package.

2.3. *Spitzer*

Additional *Spitzer* data have been used before running the neural network algorithms, especially for studying and evaluating any possible correlations between the different datasets. For this, we used HEALPix data from the two large GLIMPSE programs (I/II/3D/360/Deep/Proper/APO surveys) combined with the SMOG survey (Carey et al. 2008) at 3.6, 4.5, 5.8, and 8 μm (Churchwell et al. 2009) and MIPS GAL at 24 μm (Mizuno et al. 2008), taken from CADE, at an angular resolution of 4', and then smoothed to 5'.

2.4. SCUBA-2/JCMT

To compare our 850 μm predictions at 37'' with observational data, we used the *James Clerk Maxwell* Telescope (JCMT)/SCUBA-2 (Holland et al. 2013) 850 μm continuum observations as part of the Continuum Observations of Pre-protostellar Evolution (SCOPE) program (Eden et al. 2019). This program consisted of observations of 1235 *Planck* Galactic cold clumps. We randomly selected seven observations of this program from the EAO archive⁷, which we converted from mJy/arcsec² to MJy/sr, and smoothed from 14.4'' to 37''. The coordinates of the sources are provided in Table 1. In addition, we considered SCUBA-2 850 μm observations of M31

⁵ <https://cade.irap.omp.eu>

⁶ <https://healpix.jpl.nasa.gov/>

⁷ <https://www.eaobservatory.org/jcmt/science/large-programs/scope/>

Table 1. Central position of the JCMT/SCOPE sources used in this work.

Sources	RA	Dec
1	283.2	5.42
2	303.39	31.36
3	303.43	31.93
4	316.09	60.15
5	324.29	43.35
6	335.35	63.86
7	335.39	63.62

obtained as part of the HASHTAG Program and delivered by the consortium⁸.

2.5. Bolocam

We used Bolocam 1.1 mm data from the Bolocam Galactic Plane Survey (Aguirre et al. 2011, BGPS), at a resolution of 33'', in order to compare these with our 1.38 mm predictions. With a total coverage of 17 sq. deg, we used observations of 12 ultra-compact HII regions (UCHIIs), already used and described in Paradis et al. (2014) (see their Table 1 for the central position of the sources). Data in units of Jy/beam were converted to MJy/sr using Eq. (16) from Aguirre et al. (2011) before being convolved to an angular resolution of 37''. However, it is important to emphasize that Bolocam data suffer from noise, but also from filtering, which induces an important loss of the extended emission. For instance, 50% of the flux is attenuated for structures extending to 3.8'. For this reason, we did not include data for cold cores, for which the significant extended emission has been filtered, inducing a bad quality in the Bolocam data.

3. Correlations between multiwavelength infrared data

To decide which wavelengths are required for the neural network to be able to predict dust emission at 850 μm and 1.38 mm and which ones can be omitted, we performed a correlation analysis. Only the inner part of the Galactic plane has been observed from the NIR to the FIR using *Spitzer* and *Herschel* data. This analysis has therefore been performed using the GLIMPSE (from 3.6 to 8 μm), MIPS GAL (24 μm), and Hi-GAL (from 70 to 500 μm) surveys, smoothed to an angular resolution of 5' (see Sect. 2). To evaluate the quality of the correlations, we used the three following coefficients: Kendall (to measure the strength of the dependence between two variables), Pearson (to measure the degree of the relationship between linearly related variables), and Spearman (to measure the degree of association between two variables). The Pearson correlation is frequently used for normal distributed data, whereas Spearman’s and Kendall’s coefficients are suggested for non-normal data. The Kendall correlation is usually more robust and efficient than the Spearman correlation, especially in the case of small samples or some outliers. The results of the correlations are presented in Fig. 1 for the three coefficients. We used the Python Seaborn package to perform a hierarchically clustered heat map to facilitate the visualization of the correlations. Each case gives the correlation coefficient between the data at two different wavelengths. Since the entire dust emission spectrum increases with dust temperature, to

⁸ <https://hashtag.astro.cf.ac.uk/DR1.html>

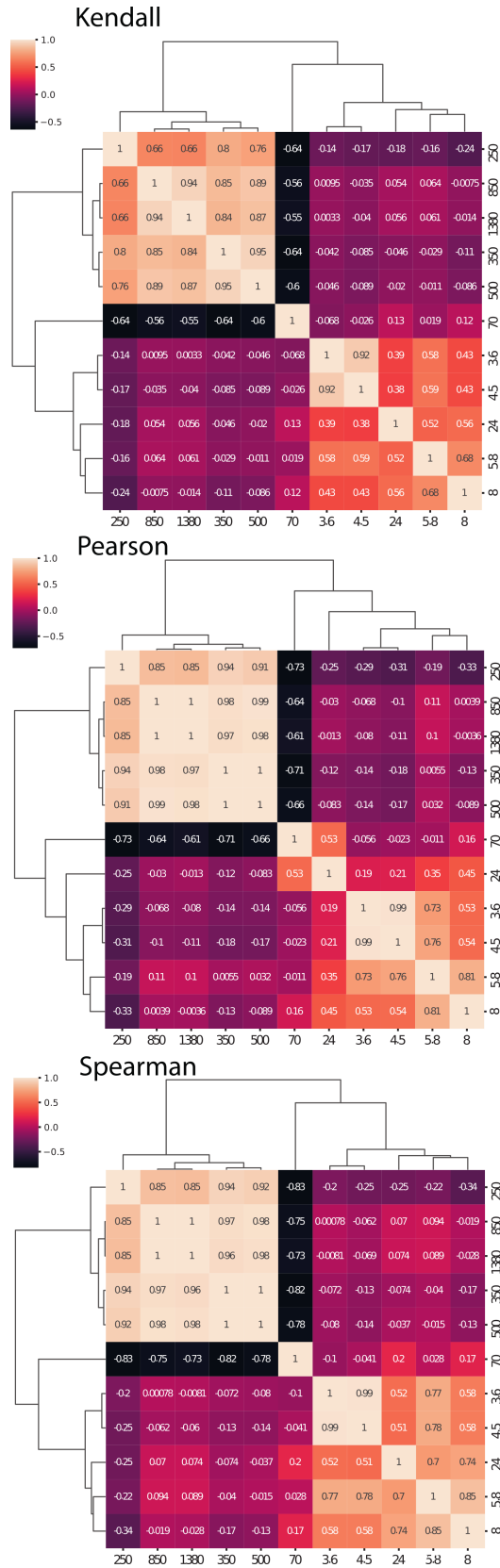


Fig. 1. Hierarchically clustered heat map of the different correlations between datasets (GLIMPSE at 3.6, 4.5, 5.8, and 8 μm ; MIPS GAL at 24 μm ; Hi-GAL from 70 μm to 500 μm , and *Planck* at 850 μm and 1.38 mm). All datasets have been smoothed to an angular resolution of 5' and normalized to the 160 μm data. Kendall, Pearson, and Spearman's correlation coefficients are given in each case.

remove this effect, which could bias the correlations, all of the data were divided by the 160 μm brightnesses. For this reason, data at 160 μm do not appear in the figure. Whichever coefficient correlation we inspect, the best correlations (with values larger than 0.66 or 0.85 depending on the coefficient) are visible for wavelengths between 250 μm and 850 μm or 1.38 mm. The coefficient values tend to decrease for wavelengths below 70 μm (with values close to 0). Emission in the NIR and the underlying processes do not affect or have a very low impact on the long-wavelength emission. The 70 μm data are primarily dominated by emission from the large grain component, but they are often contaminated by emission from smaller grains, which weakens the correlation with longer wavelengths ($\lambda > 250$ μm). The negative correlation of the $I_{\nu}(70)/I_{\nu}(160)$ ratios with the long-wavelength data arises because the 70 μm and 160 μm data lie on opposite sides of the peak of large grain emission. We therefore only consider data from 160 μm to 500 μm in the following to predict dust emission in the submm/mm using the neural network.

We note the absence of a correlation between the FIR and the MIR 24 μm . Unfortunately, in the inner Galactic plane covered by our observations, we do not have any cold clumps for which a decrease in the small grain abundance is observed in our Galaxy, probably because they stick to the largest grains or are not sufficiently heated in these dense clumps and then do not radiate. However, this behavior has not been evidenced in the Large Magellanic Cloud (LMC) clumps, for instance [Paradis et al. \(2019\)](#). Conversely, large grains should be intensively heated to have a visible effect on the 24 μm emission. Such required high temperatures (>80 K) of grains are probably not observed at an angular resolution of 5' because of dilution.

4. Neural network methodology

To create our neural network, we used a multilayer perceptron model, which consists of a supervised learning algorithm that learns a function on a dataset using multiple layers. The multilayer perceptron model is a feed-forward neural network with a structure that consists of an input layer, one or more hidden layers, and an output layer, an activation function, and a set of weights and biases. The activation function determines the output of a neuron based on its input, deciding whether a neuron should be activated or not. A neural network without any activation function becomes a linear regression model. Figure 2 shows a simple description of the neural network we use. The algorithm of our neural network consists of two phases:

- Forward propagation: the input is fed into the neural network and the result is the output from the computations applied to the data through the network.

- Back-propagation: a supervised learning technique for training a neural network. The error between the predicted output and the actual output is computed and propagated into the network. A gradient descent optimization method is used to update the weights and biases in order to reduce the error.

Our input layer consists of four neurons that are the logarithms of the data at 160, 250, 350, and 500 μm . Our two hidden layers process the information received from the input layer. The output layer is the resulting logarithm of the prediction at 850 μm or 1.38 mm. The loss function of the neural network compares the target (*Planck* data) and the predicted output values and measure the errors by giving a “loss” score. An optimizer algorithm is used to update the weights and biases in order to reduce the losses. We split our data to get 2/3 of the pixels for training the

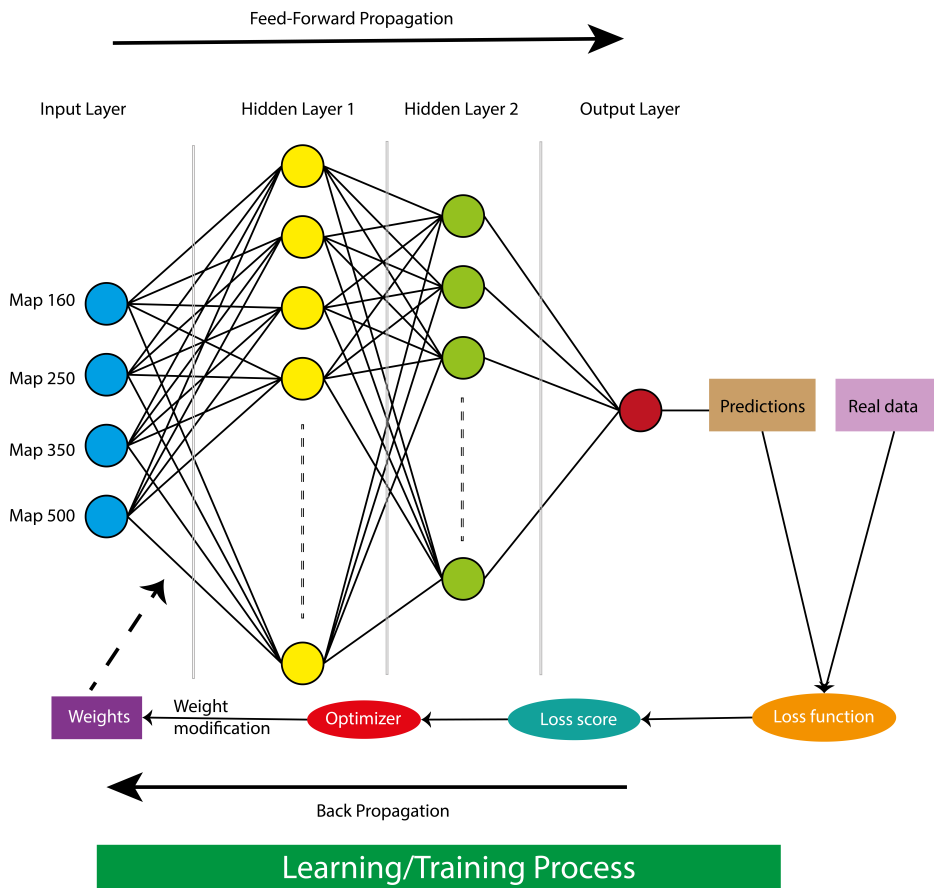


Fig. 2. Overview of a neural network for machine learning.

neural network and 1/3 for testing. We used the *tanh* activation function for all hidden layers. We implemented a custom metric function defined as the coefficient of determination R^2 , used the *Adam* optimizer with a learning rate of 0.001, and applied the *Huber* loss function.

For training, the input corresponds to the *Herschel* Hi-GAL, Gould Belt, and Cold Cores maps from 160 to 500 μm , at a 5' angular resolution. The output layer is the *Planck* 850 μm or 1.38 mm. We removed from the analysis any potential negative brightness values in the maps. The strength of this work is the important number of pixels resulting from the HEALPix format that combines a multitude of world coordinate system (WCS) fit images and that allows one to perform such a statistical analysis. Indeed, the neural network was applied on 1 242 681 independent pixels in total, with 832 596 pixels for training and 410 085 pixels for testing. Input and output maps were normalized using the *RobustScaler* function. We performed hyper-parameter tuning in order to obtain a high-performing model, which results in only two hidden layers with 12 and 8 neurons in each, respectively, to predict the 850 μm output map, and 60 and 30 neurons with the 1.38 mm output map. Applying the dropout regularization function to improve the performance of the model is not recommended in our neural network, since we do not have a large number of nodes.

5. Tools for manipulating data in the HEALPix format

All of the input data were in the HEALPix format, which is very useful to analyze a large area on the sky. However, to visualize specific regions it can be easier to extract a WCS fits file.

In addition, so far, astronomers use their own codes to extract an SED, either using the HEALPix format or the WCS one. The CADE service, created in 2012, provides astronomical data production in the HEALPix format at different resolutions, data archiving, and dissemination to the community. All the data are made to be Virtual Observatory-compatible, through the HiPS format (Fernique et al. 2015). In addition to the database, the service offers different tools for manipulating data in the HEALPix format:

- The drizzling software library⁹ (in Python), which reprojects data from HEALPix to the local WCS,
- A web interface of the Drizzlib (DrizzWeb)¹⁰,
- The first SED extractor tool¹¹ (in Python), which extracts an SED from HEALPix, WCS, or a mixture of HEALPix-WCS fits files.

In the following, we give a brief description of each tool.

5.1. World coordinate system fits file extraction

The first version of Drizzlib has been developed in the Interactive Data Language (IDL), in the framework of the *Planck* mission, to manipulate HEALPix data. The advantage of this format is that it has a unique pixelization over the entire sky, with each pixel covering the same surface area. The description of the method for the transformation from WCS fits files to HEALPix files is

⁹ <http://cade.irap.omp.eu/dokuwiki/doku.php?id=software>

¹⁰ <http://drizzweb.irap.omp.eu/>

¹¹ [http://cade.irap.omp.eu/dokuwiki/doku.php?id=sed\\$_\\$extractor](http://cade.irap.omp.eu/dokuwiki/doku.php?id=sed$_$extractor)

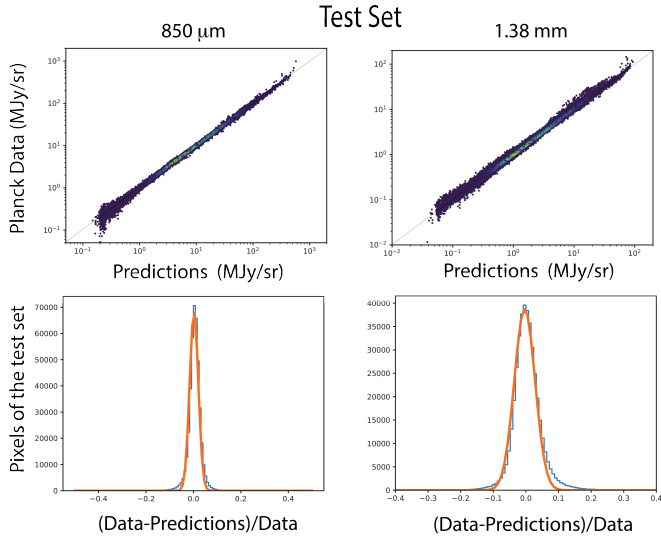


Fig. 3. Comparison between *Planck* data and predictions performed on the test set (850 μm on the left and 1.38 mm on the right). Top: Correlation plots between *Planck* data and neural network predictions. Bottom: Histograms of the relative errors between the data and neural network predictions in blue, and Gaussian fits in orange.

given in Paradis et al. (2012a) (see Appendix A). The method works in exactly the same way in the inverse transformation.

The IDL Drizzlib version has been replaced by a Python version, usable for all projections and coordinate systems. With the improvement of the resolution, the Drizzlib has been extensively modified to be able to work with HEALPix files with large NSIDE (>8192). A simplified web interface of the Drizzlib is also available online. These are the only tools able to manipulate large HEALPix files, ensuring the flux conservation from one pixelization to the other. We use a mosaicking method that computes the surface of the pixel intersections, and use these values as weights to extract the WCS fits file from the HEALPix format.

In this work, Drizzlib and DrizzWeb have extensively been used to extract WCS fits files in specific regions of the HEALPix prediction maps, for comparison with other maps or to produce an SED. The extraction time depends on the NSIDE of the original HEALPix map, as well as the size of the output WCS fits map. In the case of NSIDE = 16 384 and for output regions of several degrees (such as the Magellanic Clouds and part of the Hi-GAL region), the process takes too long. In that case, we generated HiPS of the prediction maps and extracted the WCS file using the Aladin tool. This process is acceptable for visualization only and not for data analysis, since the flux conservation is not guaranteed.

5.2. Spectral energy distribution extraction

All the SEDs presented in the following sections have been produced using the SED extractor. The SED extractor offers large flexibility in the method of extraction. The interest of such a tool is to accept WCS fits and/or HEALPix files as inputs. The conversion from one format to the other is based on the Python Drizzlib code, which ensures flux conservation. In addition, we can specify different shapes of extraction regions, allowing cuts in the coordinates limit, cuts in units of the maps, but also mixing the different possibilities. Further developments of this tool will improve the speed of the format conversion and allow for correlation plots.

We used the same regions as in Paradis et al. (2014) for extractions using *Herschel*-Bolocam data and the prediction maps; that is, using circles of 27.8'' centered on the source to compute the average brightness, and a circle annulus extended up from 27.8'' to 55.6'' to compute the median brightness in the background. As opposed to Paradis et al. (2014), in which the SEDs were generated in Jy using aperture photometry codes, we extracted SEDs in MJy/sr. The method of extraction is different as well as the considered pixels in the region and background, since some pixels are masked in the prediction maps (if relative errors are larger than 20% in the 5' maps). To compute the SED using *Herschel*-JCMT data and prediction maps, we used the same circle radius, as well as a circle annulus for the background.

In the case of M31, we produced the SED of the galaxy by averaging the brightnesses inside an ellipse centered at $(l,b) = (121.2; -21.58)$ and defined by a width of 0.55° , height of 2° , and angle inclination of 38° . We removed a background corresponding to the median brightness into a circle of 0.1° in radius centered at $(l,b) = (121.3; -20.9)$.

We considered calibration uncertainties of 7% for *Herschel* (see Balog et al. 2014, for PACS 160 μm , and the observer manual v2.4 for SPIRE), 10% for SCUBA-2 (Jenness et al. 2002), 20% for Bolocam (Ginsburg et al 2013), and 4% and 7% for predictions at 850 μm and 1.38 mm (see Sect. 6.1).

6. Dust emission predictions at 850 μm and 1.38 mm

After training the neural network, we first used as inputs the *Herschel* maps that we converted to the HEALPix format and made available on the CADE service. The maps have been smoothed to 5' (see Sect. 2.2), to be compared with the *Planck* dust emission data. Then, we used the *Herschel* HEALPix maps at an angular resolution of 37'' to predict dust emission in the *Planck* bands centered at 850 μm and 1.38 mm.

6.1. Prediction maps at 5'

We applied the best models derived from our neural networks to the Hi-GAL, Gould Belt, and Cold Cores HEALPix maps at 5'. We compare in Fig. 3 the predicted output and the *Planck* maps, restricted to the pixels used in the test set. The correlation plots show that the predicted data reproduce well the real data. There is clearly a low bias and a low variance at both wavelengths. The histograms of relative errors (see Fig. 3) indicate slightly larger relative errors for the 1.38 mm than the 850 μm . This point is not surprising, since emission at 1.38 mm can still be slightly contaminated by other emission features in the dust continuum, even after CMB, CIB, and CO removal (see Sect. 2.1). These potential contaminations can induce more complexity to recover the *Planck* dust emission data. However, for both wavelengths, the histograms are centered on values close to 0 (0.0023 and -0.0037 at 850 μm and 1.38 mm) and have small standard deviations ($\sim 4\%$ and 7% at 850 μm and 1.38 mm for 95% confidence interval).

We show the correlations for the Hi-GAL and Cold Cores programs in Figs. 4 and 5, and for all the *Herschel* programs described in Sect. 2.2 in Figs. A.1 and A.2. We removed very low-brightness pixels in the correlation plots, for all the external galaxy surveys (HERITAGE, KINGFISH, Helga, HerM33es, and VNGS). Indeed, these pixels are dominated by the noise in the data, for a brightness level below 0.05 to 0.1 MJy/sr at 1.38 mm, depending on the surveys. Again, correlations appear

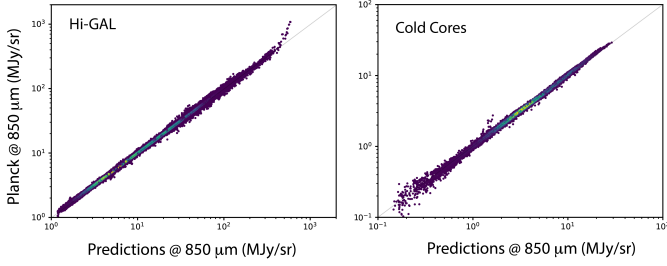


Fig. 4. Correlation plots between *Planck* data and neural network predictions at 850 μm , for the two Hi-GAL and Cold Cores *Herschel* large programs. See Fig. A.1 for the correlation plots of all the *Herschel* large programs described in Sect. 2.2.

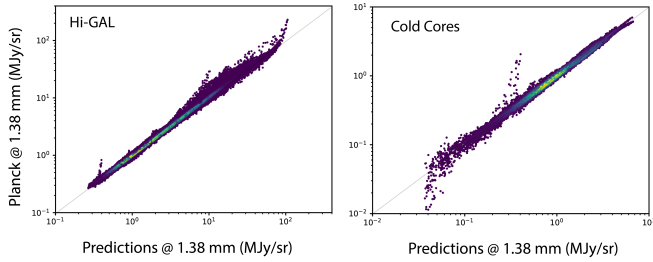


Fig. 5. Correlation plots between *Planck* data and neural network predictions at 1.38 mm, for the two Hi-GAL and Cold Cores *Herschel* large programs. See Fig. A.2 for correlation plots of all the *Herschel* large programs described in Sect. 2.2.

slightly better at 850 μm than 1.38 mm. However, we observe a systematic trend: predictions for high brightness can be underestimated (mainly in the Hi-GAL, Gould Belt, and HERITAGE programs). These very bright regions correspond to specific UCHII regions (Galactic center and Orion regions for the Milky Way (MW), and 30-Doradus for the LMC, for instance). However, these discrepancies between data and predictions only concern a few pixels (less than 0.2% in the Hi-GAL program at 1.38 mm, for instance), and are not even visible in the relative error histograms. However, to be rigorous, in the delivered maps, we removed pixels with relative errors exceeding 20%. These same regions have been removed in the prediction maps at an angular resolution of 37". The other UCHII regions do not evidence any bias in the prediction maps. This impossibility of the neural network reproducing the very bright pixels could come from two reasons. The first one is that very bright pixels represent only a few pixels and in that case the statistics may not be sufficient for the neural network to be correctly trained on these pixels. Secondly, the dust emission in these very bright masked pixels may exhibit behavior distinct from other bright regions. One possibility is a low but non-negligible contamination by free-free emission in these areas, particularly at 1.38 mm. We tried to train a distinct neural network for these specific pixels but the low statistics did not allow us to get better results. We therefore preferred to remove these pixels from the prediction maps.

Prediction maps were generated in the HEALPix format with NSIDE = 2048. We extracted some selected regions for various astronomical features (filaments, cold cores, and star-forming regions) or galaxies using the DrizzWeb interface (see Sect. 5.1). We compare predictions and observations in the Galactic plane (Fig. 6), LMC (Fig. 7), SMC (Fig. 8), M31 (Fig. 9), M33

(Fig. 10), Orion (Fig. 11), Taurus (Fig. 12), LDN1642 (Fig. 13), L134 (Fig. 14), L183 (Fig. 15), and MBM12 (Fig. 16). The relative errors between the data and the predictions are also shown in each figure. Pixels in black correspond to pixels that have been removed, either because of negative values in the inputs maps, or because of errors greater than 20% (mainly in very bright regions or, conversely, in faint noisy regions).

6.2. Prediction maps at 37"

The main goal of this work is to provide prediction maps at higher resolution (37" here) in order to analyze large regions of the sky in the submm/mm wavelength range, at the *Herschel* resolution instead of the *Planck* one. In addition, prediction maps at 37" are crucial to selecting potential regions for proposed observations with ground-based telescopes at higher resolution. The regions used to train the neural network mix different environments, with different distances and obviously different spatial scales. We do not expect to observe significant changes in the SED from an angular resolution of 5' to 37" for most regions of the Galaxy, or any significant impact from free-free emission at 1.38 mm at 37" resolution, except possibly in a few very bright regions. This is particularly true in the Orion region, where dust temperatures can reach as high as 70 K (Arab et al. 2012). However, these very bright pixels in Orion (and in a few other UCHII regions) are masked in the final maps due to their relative errors exceeding 20% (see Sect. 6.1), regardless of any potential contamination. A strong contribution of free-free emission could occur at angular resolutions of a few arcseconds.

We therefore consider that the regions we used from training the neural network reveal a large diversity of dust emission spectra that could be representative of the overall of dust emission properties at long wavelengths. In consequence, we applied the parameters of the neural network that give the best agreement with the *Planck* data to the 37" *Herschel* input maps. These new prediction maps (with NSIDE = 16 384) are presented in all previous figures (from Figs. 6 to 16). This way, we can clearly see the benefit of a better angular resolution, compared to the *Planck* one.

We next compare the prediction maps with available ground-based data, from the JCMT/SCUBA-2 850 μm and Bolocam data at 1.1 mm. Because of the filtering, we compare brightnesses in aperture photometry after removing the same background in each maps.

6.2.1. Comparison of cold core predictions with JCMT/SCUBA-2

Figure 17 presents the extracted SED for each source (see Sect. 5.2). An additional modified black-body fit was adjusted to give a simple view of the spectral shape of the SEDs. The difference between JCMT 850 μm data and the predictions is less than 10% for most of the source; therefore, the data and predictions are compatible within the error bars, except for one source that evidences a difference of less than 30%. The comparison is nevertheless impressive, with the 37" predictions and JCMT data showing similar brightnesses. This agreement suggests that the dust emission behavior observed at an angular resolution of 5' across a wide range of pixels with various physical conditions can be reliably reproduced at sensibly higher resolution. However, predictions at 850 μm do not systematically follow the modified black-body emission model. For instance, one source (RA = 303.43; Dec = 31.93) shows a 850 prediction that falls below the fit, while predictions for two other sources

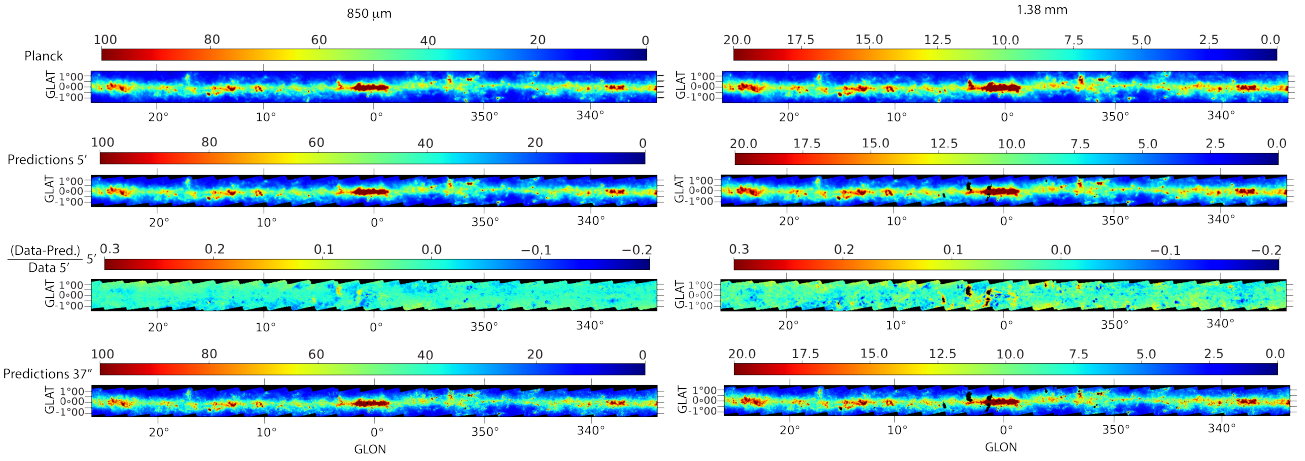


Fig. 6. Comparison between *Planck* data and predictions for a portion of the Galactic plane, at 850 μm on the left and 1.38 mm on the right. From top to bottom: *Planck* data (5' angular resolution), neural network predictions (5'), relative error between data and predictions (5'), and neural network predictions (37'').

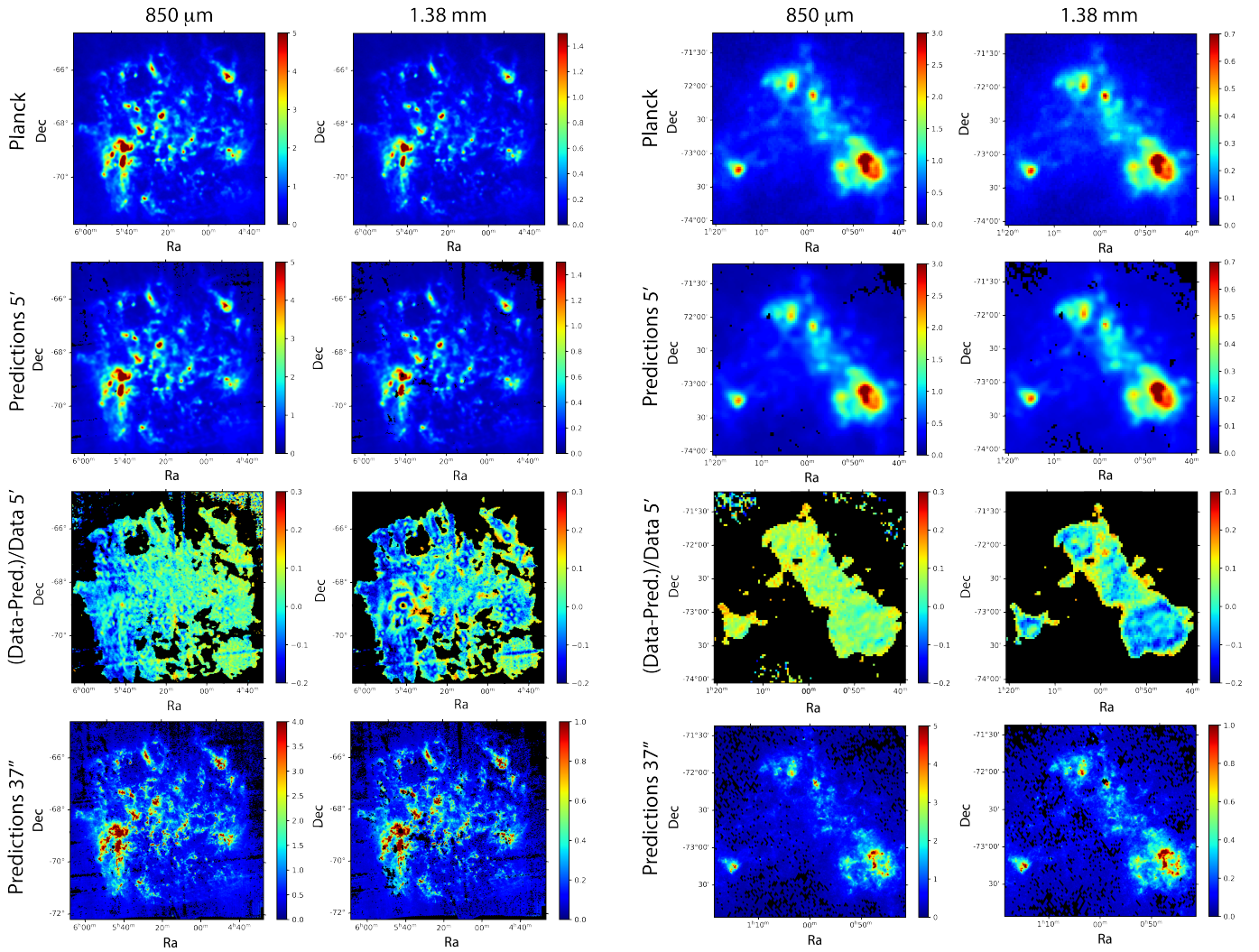


Fig. 7. Comparison between *Planck* data and predictions for the LMC, at 850 μm on the left and 1.38 mm on the right. From top to bottom: *Planck* data (5' angular resolution), neural network predictions (5'), relative error between data and predictions (5'), and neural network predictions (37'').

Fig. 8. Comparison between *Planck* data and predictions for the SMC, at 850 μm on the left and 1.38 mm on the right. From top to bottom: *Planck* data (5' angular resolution), neural network predictions (5'), relative error between data and predictions (5'), and neural network predictions (37'').

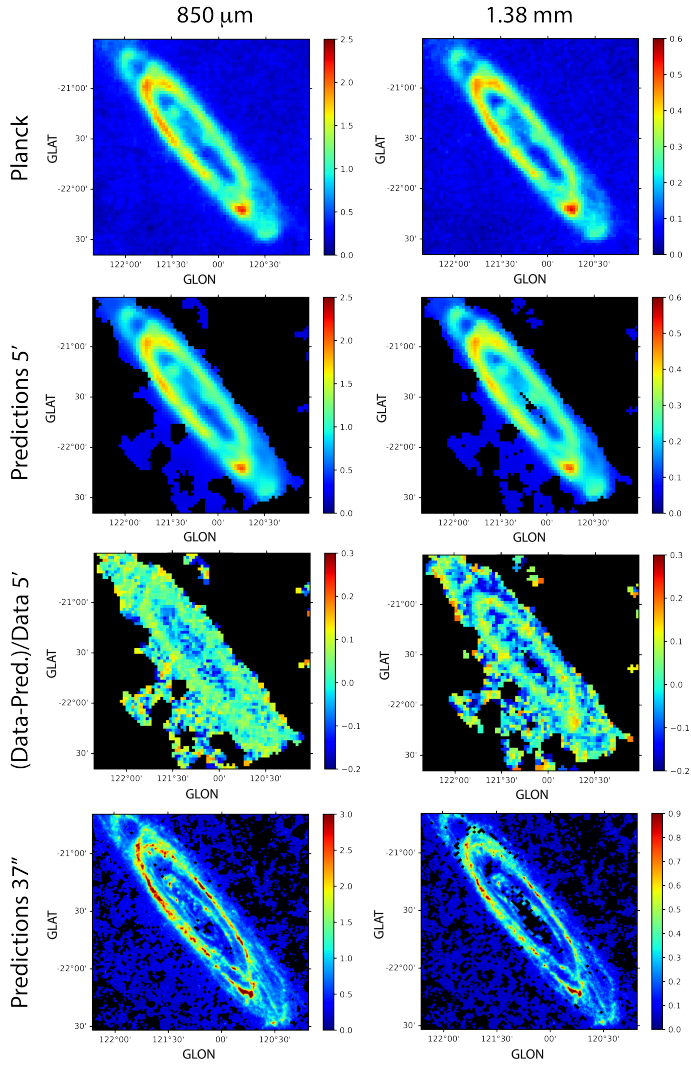


Fig. 9. Comparison between *Planck* data and predictions for M31, at 850 μm on the left and 1.38 mm on the right. From top to bottom: *Planck* data (5' angular resolution), neural network predictions (5'), relative error between data and predictions (5') and neural network predictions (37'').

(RA = 316.09; Dec = 60.15 and RA = 324.29; Dec = 43.35) appear to slightly exceed the fit. The low JCMT brightness of one source is probably due to an inaccurate flux calibration. For instance, the 450 μm cannot be used due to its low accuracy in the flux calibration.

6.2.2. Comparison of UCHII regions predictions with Bolocam

To compare the 1.38 mm prediction maps with observational data, we used Bolocam data at 1.1 mm. However, these data suffer from an important attenuation of the extended emission. For that reason, data from UCHII regions (except perhaps from the Galactic center, Orion bar, and 30-Doradus) should be more reliable, since they are compact and their emission largely dominates any potential contribution from the extended emission. The comparison is given in Fig. 18 for four UCHII regions, and in Fig. A.3 for the 12 UCHII regions of this study. Except for one UCHII region, the Bolocam data are most of the time slightly below the modified black-body fit. Only three SEDs

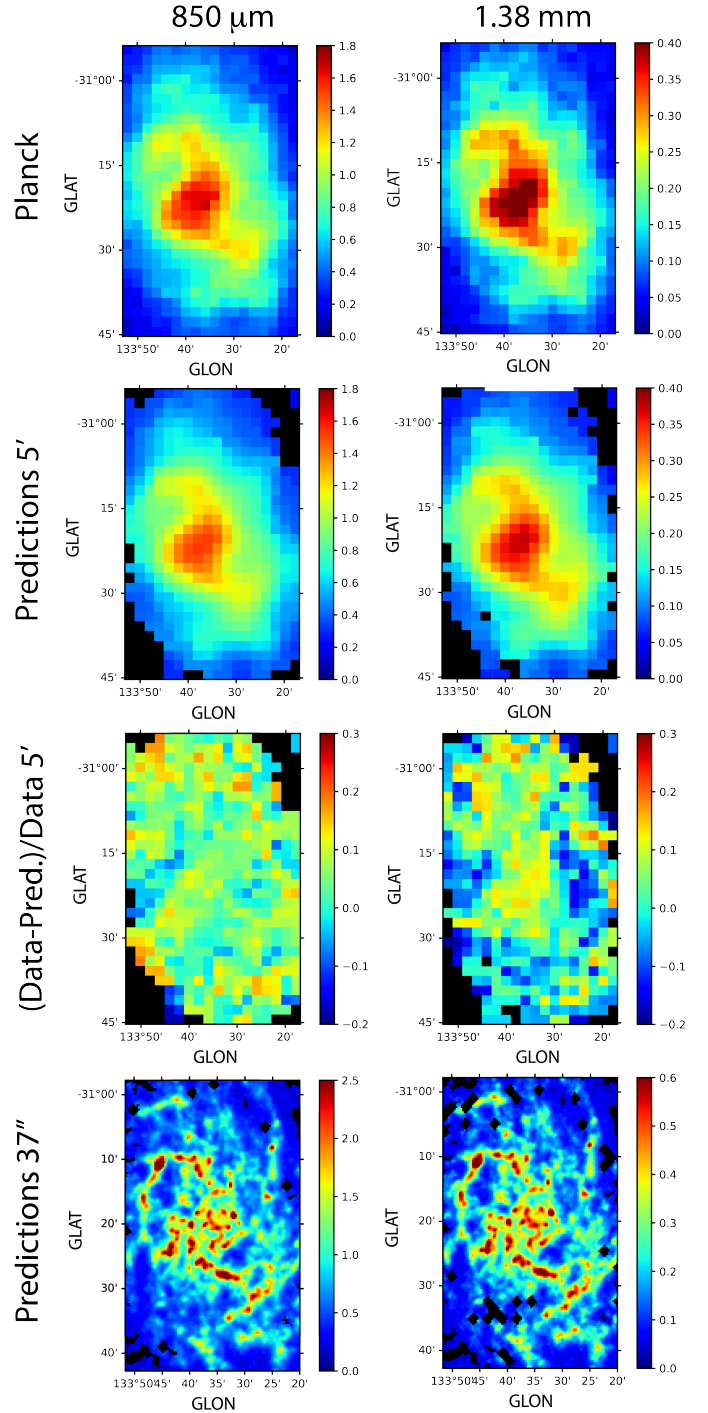


Fig. 10. Comparison between *Planck* data and predictions for M33, at 850 μm on the left and 1.38 mm on the right. From top to bottom: *Planck* data (5' angular resolution), neural network predictions (5'), relative error between data and predictions (5') and neural network predictions (37'').

of UCHII show a significant difference between Bolocam and the fits (17 279, 18 469, and 18 502). For the rest of the UCHII regions, the comparison is quite favorable and strongly suggests a compatibility between the predictions and Bolocam data. And again, these results confirm the reliability of the prediction maps. Furthermore, the prediction maps do not suffer from filtering, or from other data processing artifacts, and therefore can bring a lot of advantages and reliability when compared to ground-based data.

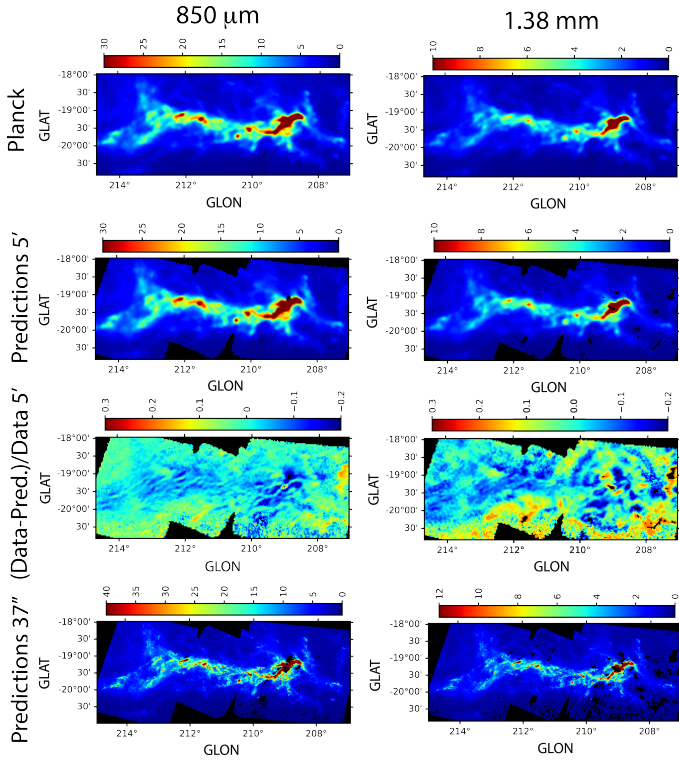


Fig. 11. Comparison between *Planck* data and predictions for the Orion region, at 850 μm on the left and 1.38 mm on the right. From top to bottom: *Planck* data ($5'$ angular resolution), neural network predictions ($5'$), relative error between data and predictions ($5'$) and neural network predictions ($37''$).

6.2.3. Prediction map delivery

The prediction maps generated at angular resolutions of $5'$ and $37''$ are provided on the CADE website¹², as well as the *Planck* data at 850 μm and 1.38 mm after CMB, CIB, and CO removal (see Sect. 2.1).

7. Discussion

7.1. From the $I_\nu(850)/I_\nu(1380)$ ratio to the spectral index and dust emissivity index

We first computed the $I_\nu(850)/I_\nu(1380)$ ratios derived from *Planck* data for each survey, and derived from the prediction maps at $37''$. The histograms and Gaussian fits of the Hi-GAL and Cold Cores programs are shown in Fig. 19, and of all the programs described in Sect. 2.2 in Figure A.4. The first difference appears for the Hi-GAL and Gould Belt surveys, which evidence distinct histograms: a Gaussian profile in the case of *Planck* data, and a double Gaussian profile in the case of predictions. This difference does not come from the resolution, because we observe the same histograms when using predictions at $5'$ (not shown in the paper), but rather from an intrinsic effect of the neural network. The neural network slightly modified the peak of the $I_\nu(850)/I_\nu(1380)$ histogram ratio. This effect is the result of small variations of a few percent in the predictions compared to the data. The two peaks in the prediction

¹² <https://cade.irap.omp.eu/dokuwiki/doku.php?id=nnpredictions>

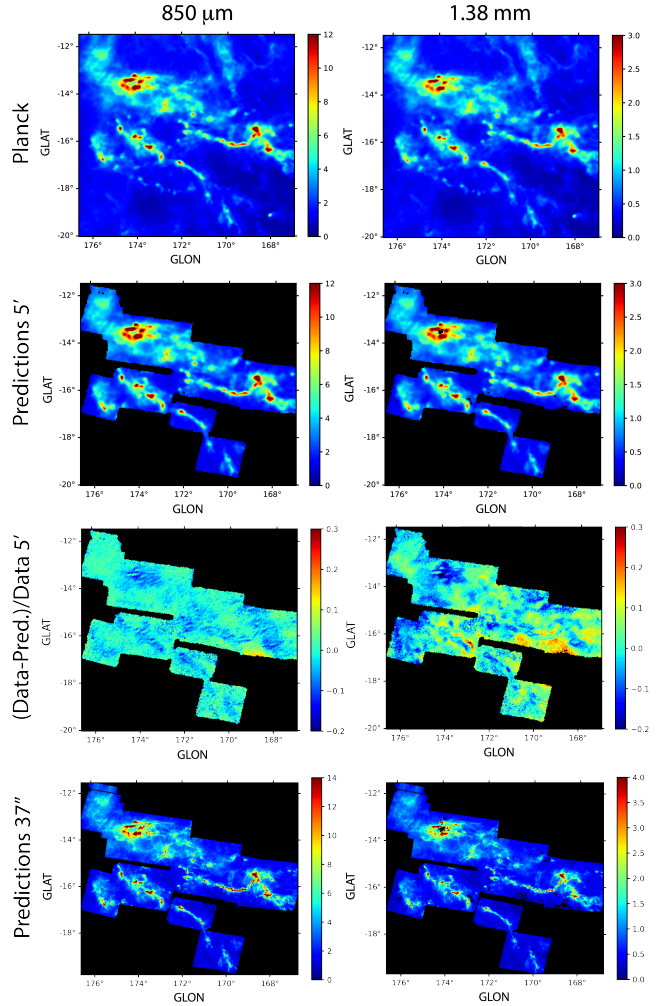


Fig. 12. Comparison between *Planck* data and predictions for the Taurus region, at 850 μm on the left and 1.38 mm on the right. From top to bottom: *Planck* data ($5'$ angular resolution), neural network predictions ($5'$), relative error between data and predictions ($5'$) and neural network predictions ($37''$).

histogram correspond to a decrease or increase of a few percent ($\sim 3\text{--}4\%$ compared to the single peak centered at 4.29 in the *Planck* histogram of Hi-GAL at $5'$, for instance) induced by the neural network, which is negligible. In the other cases, the $37''$ prediction histograms show narrower profiles, except for the VNGS survey, which exhibits the opposite behavior, likely due to there being significantly fewer pixels in the histograms. These differences in histogram profiles result from an inherent effect of the neural network. The extreme dispersion of the ratio is approximately 13% at the full width at half maximum (in the VNGS histograms). However, the most important result here is that the central values of the histograms are quite similar for all environments (see the μ values in the figure). This means that statistically the ratio is between 4 and 4.3. From a general point of view, the mean slope in the submm-mm wavelength range is statistically the same whatever the environment, indicating a certain stability in the dust emission spectrum at long wavelengths. We note however that the most diffuse part of the Galactic ISM, used to derive the “standard” Galactic SED, is not represented in this analysis.

We computed the observed spectral index, $\alpha_{850\text{--}1380\mu\text{m,obs}}$, for all *Herschel* large programs using *Planck* data at $5'$,

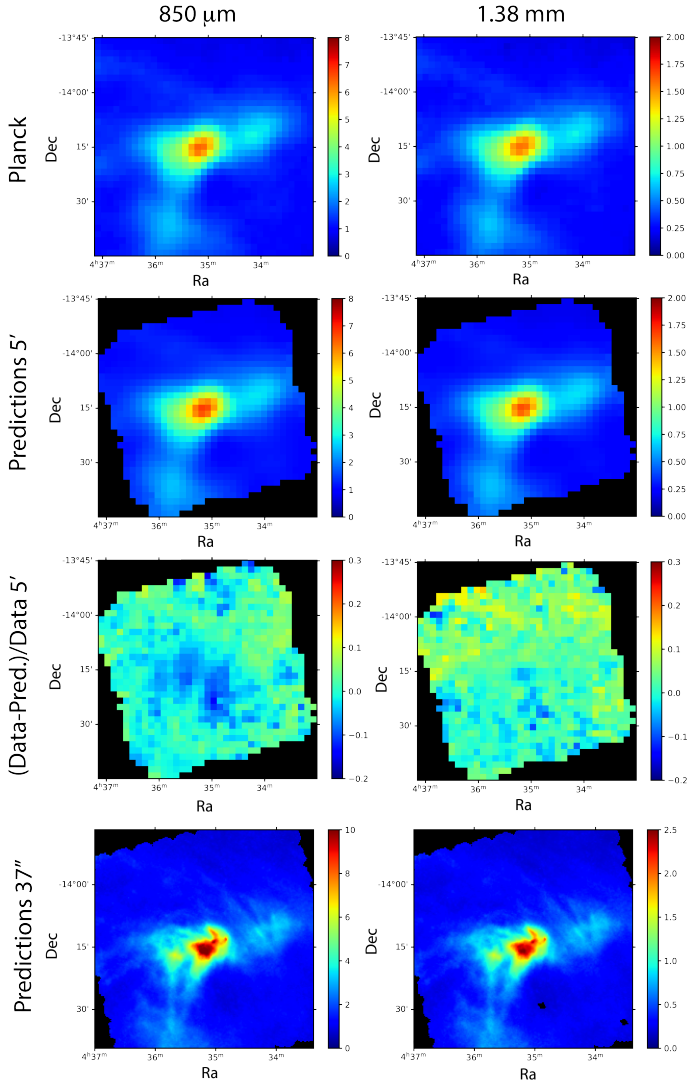


Fig. 13. Comparison between *Planck* data and predictions for LDN1642, at 850 μm on the left and 1.38 mm on the right. From top to bottom: *Planck* data (5' angular resolution), neural network predictions (5'), relative error between data and predictions (5') and neural network predictions (37'').

defined as

$$\alpha_{850-1380 \mu\text{m}} = \frac{\log(I_{\nu}(850)/I_{\nu}(1380))}{\log(850/1380)}. \quad (1)$$

Assuming optically thin emission at long wavelengths and in the Rayleigh-Jeans approximation, we can deduce the dust emissivity index (β^*) by using this simple relation: $\beta^* = \alpha - 2$. For simplicity, we note β^* , the dust emissivity index derived from the $I_{\nu}(850)/I_{\nu}(1380)$ ratio, compared to the standard β derived from a temperature (T)-spectral index (β) model. We obtain $\beta_{850-1380 \mu\text{m}}^*$ values around 1, which indicates a low emissivity index at long wavelengths. Table 2 gives the correspondence between $I_{\nu}(850)/I_{\nu}(1380)$ and $\beta_{850-1380 \mu\text{m}}^*$ for the central value (μ) of each histogram. However, we note that computing $\beta_{850-1380 \mu\text{m}}^*$ using predictions (at 37'' or 5') can be biased by the neural network due to variations in the histogram profiles (see above). These variations could lead to a change of spectral index up to +0.25 in extreme cases, observed in the VNGS survey. Statistically, several analyses evidenced significantly higher β values at

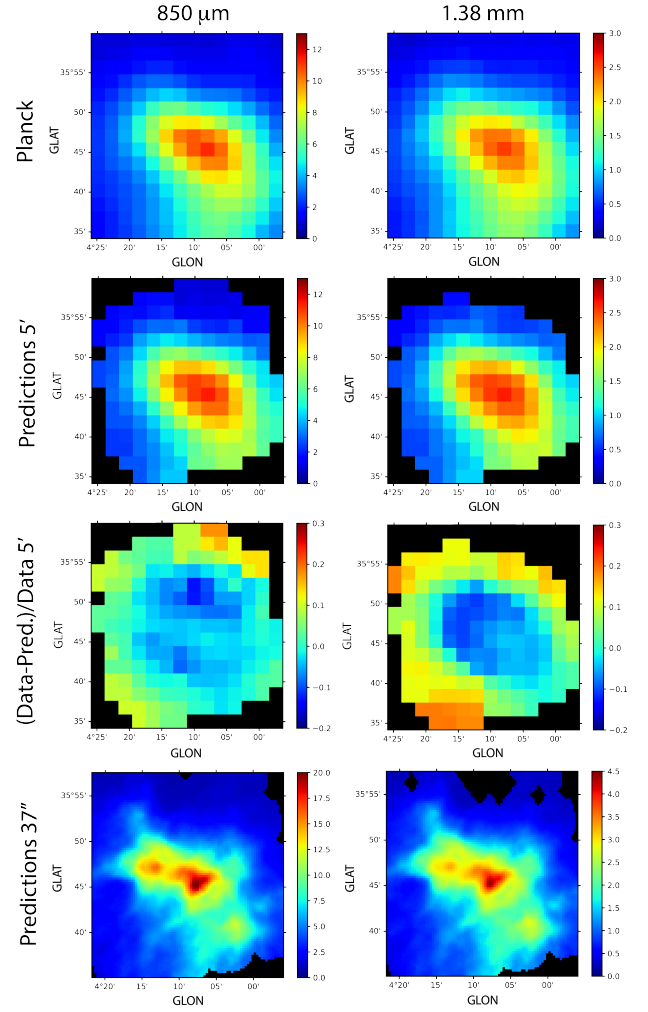


Fig. 14. Comparison between *Planck* data and predictions for L134, at 850 μm on the left and 1.38 mm on the right. From top to bottom: *Planck* data (5' angular resolution), neural network predictions (5'), relative error between data and predictions (5') and neural network predictions (37'').

Table 2. Correspondence between the intensity ratio derived from *Planck* (5') and the dust emissivity index.

Region	$I(850)/I(1380)$ <i>Planck</i> (5')	$\beta_{850-1380 \mu\text{m}}^*$
Hi-GAL	4.289	1.005
Cold Cores	4.130	0.927
Gould Belt	4.110	0.917
Heritage	4.198	0.960
HerM33es	4.202	0.962
Helga	4.247	0.984
KINGFISH	4.122	0.922
VNGS	3.960	0.840

shorter wavelengths (see for instance [Stepnik et al. 2003](#); [Abergel et al. 2010](#); [Paradis et al. 2010](#); [Juvela et al. 2011](#)) – that is, in the FIR wavelength range – meaning that a break in the spectral shape in the dust emission spectrum is a realistic assumption, as has already been proposed by several authors (see for instance [Mény et al. 2007](#); [Paradis et al. 2009](#); [Juvela et al. 2015](#)).

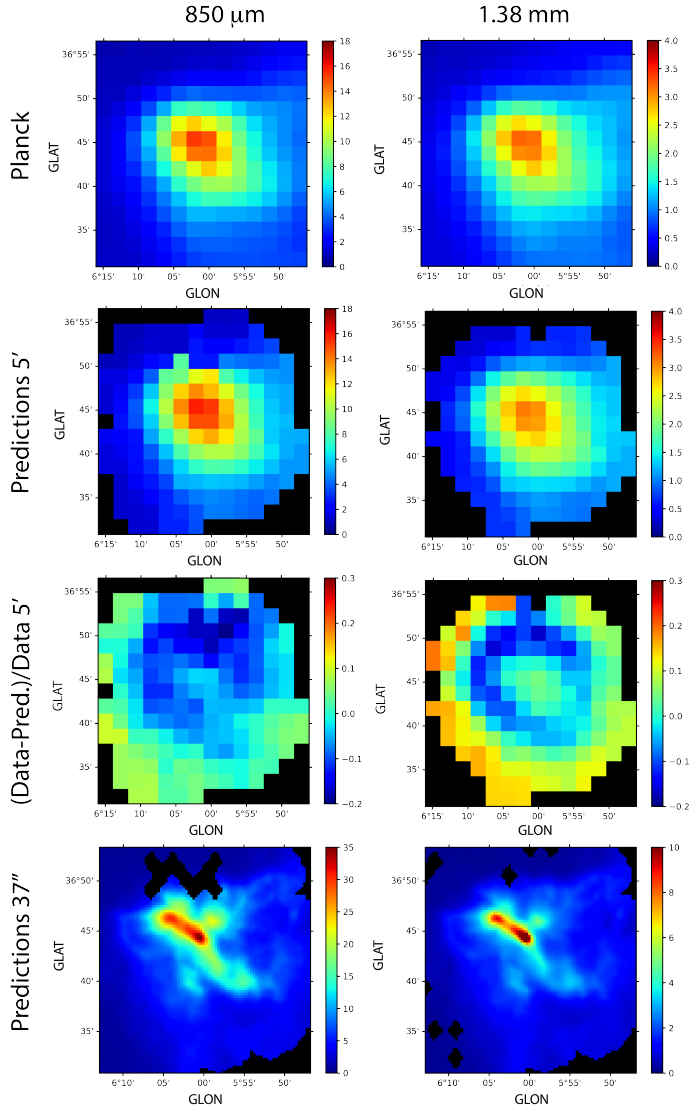


Fig. 15. Comparison between *Planck* data and predictions for L183, at 850 μm on the left and 1.38 mm on the right. From top to bottom: *Planck* data (5' angular resolution), neural network predictions (5'), relative error between data and predictions (5') and neural network predictions (37'').

Reach et al. (1995) tried to explain the flattening in the COBE/FIRAS spectrum (Fixsen et al. 1994) of the diffuse ISM. They found a good fit to the data, with the use of a two modified black-body model with dust populations at $\sim 16\text{--}21$ K and $\sim 4\text{--}7$ K. The authors, however, argued against the existence of such a cold dust component. Finkbeiner et al. (1999) also provided a two-component dust model, in which the components are described by two distinct emissivity spectral indices. This model required amorphous silicate grains at 9.5 K ($\beta = 1.7$) and carbonaceous grains at around 16 K ($\beta = 2.7$). The *Planck* 2014 data release was analyzed by Meisner and Finkbeiner (2015), who proposed an update of the Finkbeiner et al. (1999) model, with best temperatures of 15.7 K ($\beta = 2.82$) and 9.75 K ($\beta = 1.63$), as a better model than the *Planck* Collaboration XI (2020) model ($T = 19.74$ K, $\beta = 1.6$).

Adding long-wavelength data (in the mm range) usually decreases the global β value, mainly in the diffuse medium (see for instance *Planck* Collaboration Int. XVII 2014). However,

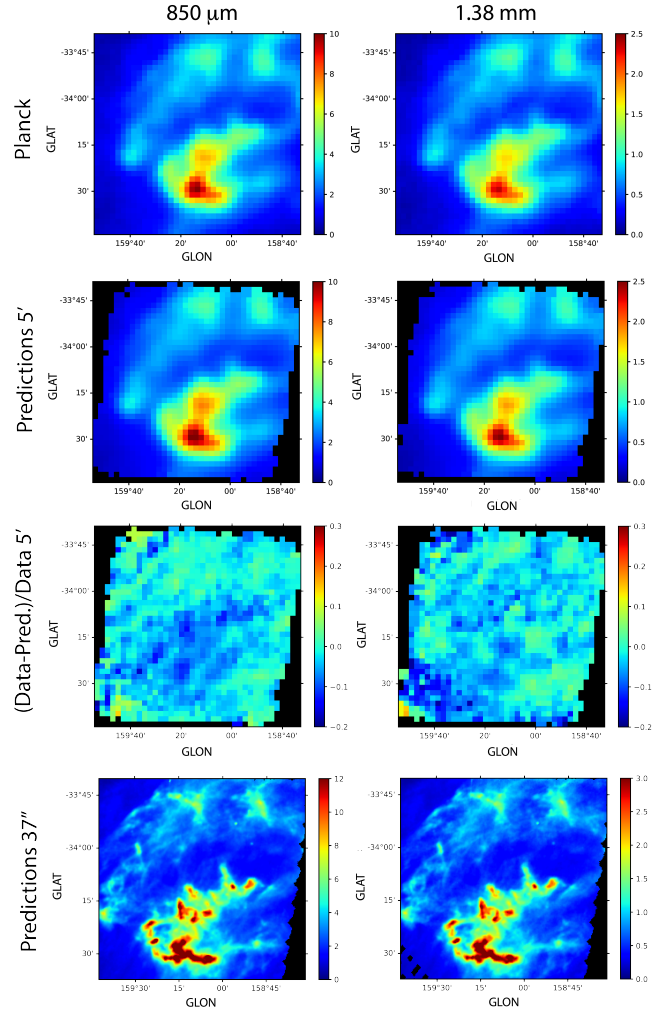


Fig. 16. Comparison between *Planck* data and predictions for MBM12, at 850 μm on the left and 1.38 mm on the right. From top to bottom: *Planck* data (5' angular resolution), neural network predictions (5'), relative error between data and predictions (5') and neural network predictions (37'').

β values have always been derived including FIR wavelengths, which induces an increase in β compared to the use of the submm-mm range only. This work reinforces the idea that the dust emissivity spectral index could be wavelength-dependent, as has been observed in laboratory experiments (see for instance Agladze et al. 1994, 1996; Mennella et al. 1998; Boudet et al. 2005; Coupeaud et al. 2011; Demyk et al. 2017a,b). However, thermal free-free emission of ionized gas could also be responsible for this behavior by contaminating the submm-mm data. For instance, Izotov et al. (2014) studied dust emission in a large sample of emission-line star-forming galaxies. They found important free-free emission of ionized gas in the submm and mm range that could cause the submm excess, as was discussed by Rémy-Ruyer et al. (2013). Lisensfeld et al. (2002) and Galliano et al. (2005) also analyzed the contamination by free-free emission in dwarf galaxies and identified a contribution that can reach 13% of the emission at 850 μm and 23% at 1.2 mm. However, in the Magellanic Clouds, the different components such as free-free, synchrotron, and foreground emissions do not really affect the 850 μm and 1.38 emissions in the LMC and SMC SEDs after

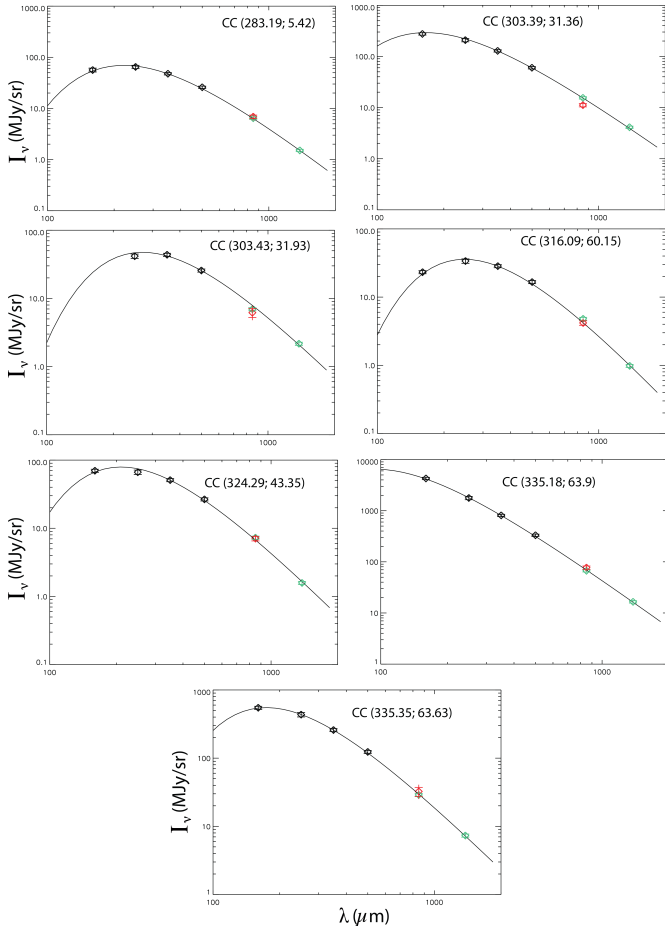


Fig. 17. SEDs of Cold Cores (Galactic coordinates given in the parenthesis), with *Herschel* data (from 160 to 500 μm) in black, JCMT (850 μm) in red, and predictions (850 and 1380 μm) in green. A modified black-body fit is shown for convenience.

CMB subtraction (see Table 2 in [Planck Collaboration XVII 2011](#)). Their contribution may affect the SED at longer wavelengths. In addition, we do not expect to observe free-free nor synchrotron emission in cold cores. If the low emissivity index were the result of these additional components, we would therefore statistically expect to observe important variations from one environment to the other, which is not the case.

Moreover, $\beta_{850-1380\ \mu\text{m}}^*$ seems to be much lower than has previously been thought. For instance, [Planck Collaboration XI \(2020\)](#) derived a mean spectral index of 1.62 over the whole sky using a modified black-body model between 100 and 850 μm . First, this value of β is highly temperature-dependent with this model, as well as uncertainty-dependent, and was computed on a shorter wavelength range compared to our analysis, which could explain a higher value. Nevertheless, looking at their Fig. 9, we observe β values going from ~ 1.2 to 2.2 along the Galactic plane, and with high values in the inner Galactic plane. Our lower value could be recovered assuming a flattening of the dust emission spectrum for wavelengths larger than 850 μm . [Planck Collaboration Int. XVII \(2014\)](#) confirm this behavior by comparing the β_{mm} ($\lambda > 850\ \mu\text{m}$) with the β_{FIR} . We note, however, that the $\beta_{850-1380\ \mu\text{m}}^*$ that we obtain is a strict value derived from a brightness ratio and does not take any uncertainty into account. The inclusion of FIR data that requires knowing the dust temperature would probably induce a higher β value. If we compute

$\beta_{850-1380\ \mu\text{m}}^*$ in the LMC and SMC derived from the global SED using *Planck* data from [Planck Collaboration XVII \(2011\)](#) (see their Table 2), we get values of 1.02 and 0.67 in the LMC and SMC, respectively, significantly lower than the values derived from a T- β model applied from FIR to mm wavelengths, which are 1.5 and 1.2, respectively. For the SMC, the authors observed a significant flattening of the dust emission for $\lambda > 850\ \mu\text{m}$ that could explain the lower value of $\beta_{850-1380\ \mu\text{m}}^*$ based on the $I_{\nu}(850)/I_{\nu}(1380)$ ratio. For the LMC, we note that β derived from a T- β fit is not well constrained when looking at the χ^2 values, and is highly degenerate with the dust temperature value.

For M33, [Tibbs et al. \(2018\)](#) recovered an effective dust emissivity index derived from the 100 μm to 3 mm data going from 0.93 to 1.44 depending on the CMB-subtraction method, whereas, using their *Planck* brightness values, we computed $\beta_{850-1380\ \mu\text{m}}^*$ between 0.87 and 1.1. For the same galaxy, we find $\beta_{850-1380\ \mu\text{m}}^*$ of 0.98 using values from [Hermelo et al. \(2016\)](#) (see their Table 2).

We can conclude that the dust spectral index seems to vary with wavelength, with a FIR dust emissivity index that could be significantly higher than its value at long wavelengths. However, at a different spatial scale and in particular at an angular resolution of a few arcseconds, we do not know if this spectral behavior can still occur.

7.2. Predicting dust emission in nearby extragalactic environments

One of the most impressive results is that even if the neural network has been trained on Galactic data only (Hi-GAL, Gould Belt, and Cold Cores), it is able to predict dust emission in other nearby galaxies, and in the Magellanic Clouds in particular (Figs. 7 and 8). The Magellanic Clouds are two of the nearest galaxies and as such are easily resolved by observations. These galaxies are characterized by a lower metallicity compared to the MW ($\frac{1}{2}Z_{\odot}$ and $\frac{1}{5}Z_{\odot}$ for the LMC and SMC, [Russel and Dopita 1992](#)). The physical conditions in the Magellanic Clouds are different from the MW: the radiation field is higher ([Dufour 1984; Lequeux 1984](#)), the filling factor of dense clouds is lower in the Magellanic clouds than in the MW ([Pineda et al. 2012](#)), and the average dust emission spectrum appears significantly flattened in the FIR-submm range in the LMC and even more in the SMC ([Israel et al. 2010; Bot et al. 2010; Rémy-Ruyer et al. 2013](#)). Therefore, it is accepted that the dust properties differ from those of Galactic dust, though the origin of this difference remains unexplained. Each model that has its own dust properties (abundances, sizes, optical properties, etc.) can always reproduce (more or less) the NIR to submm/mm data by changing the parameters ([Chastenet et al. 2017; Paradis et al. 2023](#)). It is possible to interpret the emissivity variations in the framework of one model and reproduce them by changing the parameters, but in the end we are not able to determine the dust emission brightness at a specific wavelength for a given region of the sky. Conversely, the neural network seems to be able to predict the dust emission in various environments by analyzing only the dust spectral behavior between 160 μm and 500 μm . That means that the submm/mm emission is fully predictable using the FIR domain. Therefore, the submm excess already appears in the FIR wavelength range. For instance, several analyses explored the 500 μm excess ([Paradis et al. 2012b; Gordon et al. 2014; Rémy-Ruyer et al. 2013](#)), which is also a crucial wavelength at which a change in the emissivity spectral index with wavelengths was reported in the framework of dust modeling ([Mény et al. 2007](#)).

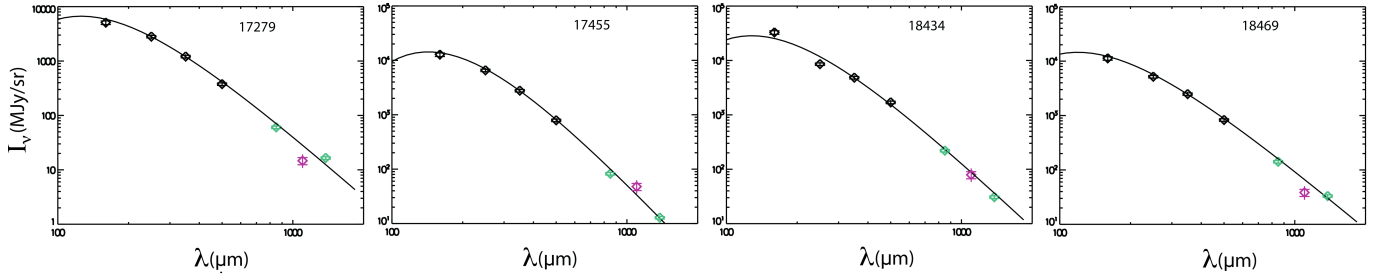


Fig. 18. SEDs of four UCHII regions (coordinates given in [Paradis et al. 2014](#)), with *Herschel* data (from 160 to 500 μm) in black, Bolocam (1.1 mm) in pink, and predictions (850 and 1380 μm) in green. A modified black-body fit is shown for convenience. See Fig. A.3 for the SEDs of the 12 UCHII regions described in Sect. 2.5 and in [Paradis et al. \(2014\)](#).

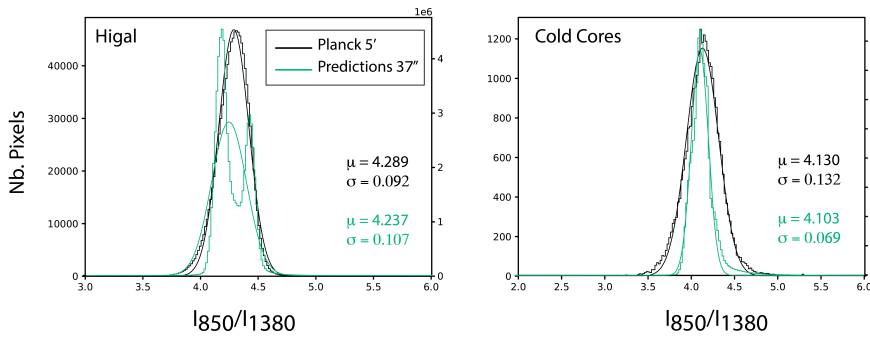


Fig. 19. Histograms of the $I_{\nu}(850)/I_{\nu}(1380)$ ratio for the two Hi-GAL and Cold Cores *Herschel* large programs, deduced from the *Planck* data at 5' in black, and from the predictions at 37'' in green. Gaussian fits are overplotted, with the central values (μ) and the standard deviations (σ) given in each panel. The left and right y axes in each panel correspond to the number of pixels for the *Planck* data and prediction histograms. See Fig. A.4 for histograms of all the *Herschel* large programs described in Sect. 2.2.

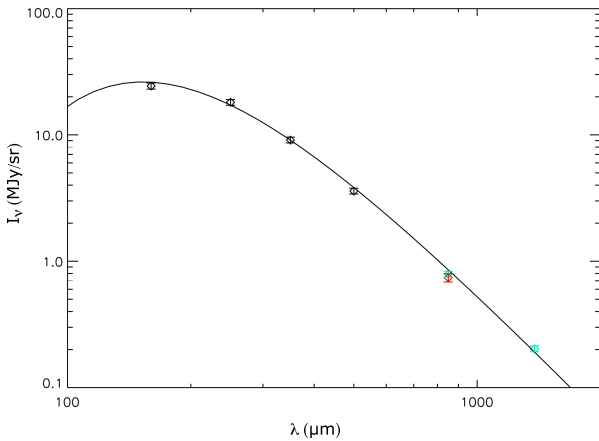


Fig. 20. SED of M31, with *Herschel* data (from 160 to 500 μm) in black, JCMT (850 μm) in red, and predictions (850 and 1380 μm) in green. A modified black-body fit is shown for convenience.

In a similar way, predictions at 5' are very convincing for M31 and M33 (Figs. 9 and 10). Several analyses of dust emission in M31 and M33 did not converge on the variation in the dust opacity index in dense environments using *Herschel* images. [Tabatabaei et al. \(2014\)](#) showed a decrease in the spectral index with galactocentric distance in M33, whereas [Smith et al. \(2012\)](#) evidenced the opposite behavior as a function of radius in M31, both with *Herschel* data and a similar linear resolution. This discrepancy could be the result of the degeneracy between the dust temperature and the spectral index in M31, as was pointed out by [Tabatabaei et al. \(2014\)](#). This point shows the complexity of understanding the dust emission behavior, and so of determining the dust temperature and dust masses. With the lack of long-wavelength data at the *Herschel* resolution, no one is capable of predicting the spectral behavior of the dust emission in the mm range.

The SED of M31 combining *Herschel*, SCUBA-2, and predictions is given in Fig. 20. We can note that predictions at 850 μm are in very good agreement with SCUBA-2 data. This confirms again the goodness of the calculated prediction maps. Moreover, these maps do not suffer from extended emission filtering; the noise level is also significantly reduced compared to ground-based data. Prediction maps of the KINGFISH survey also evidence good agreement when comparing with *Planck* data in Figs. A.1 and A.2. Comparisons with the VNGS predictions show, however, some discrepancies for a few pixels that have then been removed in the final maps produced.

If the neural network is able to predict emission in any region of the sky, this means that the spectral behaviors of the dust emission in the FIR-mm are not necessarily too different from one nearby galaxy to another. Whatever the composition of the large dust grains and their dust properties, their spectral behaviors are included in the FIR-mm global emission and can be reproduced across various environments. Or, within a simple hypothesis, the large dust components could have similar dust properties in our Galaxy and in some nearby extragalactic environments, but their proportions could spatially vary.

8. Conclusions

By applying neural networks to large datasets from the *Herschel* and *Planck* missions, we have produced, for the first time, prediction maps of dust emission at a 37'' angular resolution, in the two *Planck* bands centered at 850 μm (353 GHz) and 1.38 mm (217 GHz). We are making these maps available to the community through the CADE service, covering surveys such as Hi-GAL, Cold Cores, Gould Belt, Magellanic Clouds, M33, M31, KINGFISH, and VNGS. We estimate the uncertainties on these predictions to be approximately 4% at 850 μm and 7% at 1.38 mm. Although the supervised deep learning algorithms were trained primarily on Galactic environments, the neural networks are also capable of accurately reproducing data from

nearby extragalactic environments. This impressive result suggests that variations in dust properties could be reproducible across different regions of the sky, provided that appropriate training datasets are used. In that sense, the spectral behaviors of the FIR to the mm dust emission are similar in Galactic and nearby extragalactic environments.

The prediction maps have been compared with JCMT/SCUBA-2 observations at 850 μm , as well as with Bolocam data at 1.1 mm. The agreement between predictions and SCUBA-2 data is very good (less than 10% for most of the sources and within the error bars). Bolocam data are also compatible with predictions of UCHIIIs. Another important result is the low spectral index between 850 μm and 1.38 mm, statistically close to 1, which could support the hypothesis that dust emission flattens at long wavelengths.

The large spatial coverage of the prediction maps will help in statistically probing the dust emission variations at long wavelengths in specific regions due to the important benefit for the angular resolution compared to *Planck*. In addition, these maps could play the role of first templates of dust emission at this resolution in the framework of foreground subtraction. Moreover, they will help in preparing future observations at high angular resolutions. The powerful capabilities of neural networks could allow future analyses to make predictions in different regions of the sky, and/or at other wavelengths. As a second step, it would be promising to apply deep learning techniques, including convolutional neural networks, to recover the best angular resolution of the data used in the process.

Acknowledgements. We acknowledge the referee for his constructive and valuable comments. We acknowledge the use of data and analysis softwares provided by the Centre d'Analyse de Données Etendues (CADE), a service of IRAP-UPS/CNRS (<http://cade.irap.omp.eu>). DP acknowledges Emmanuel Caux and Philippe Garnier for fruitful discussions on Machine Learning.

References

- Abergel, A., Arab, H., Compiègne, M., et al. 2010, *A&A*, 518, L96
- Agladze, N. I., Sievers, A. J., Jones, S. A., et al. 1994, *Nature*, 372, 243
- Agladze, N. I., Sievers, A. J., Jones, S. A., et al. 1996, *ApJ*, 462, 1026
- Aguirre, J. E., Ginsburg, A. G., Dunham, M. K., et al. 2011, *ApJS*, 192, 4
- André, P., Men'shchikov, A., Bontemps, S., et al. 2010, *A&A*, 518, L102
- Arab, H., Abergel, A., Habart, E., et al. 2012, *A&A*, 541, A19
- Balog, Z., Müller, T., Nielbock, M., et al. 2014, *ExA*, 37, 129
- Bendo, G. J., Boselli, A., Dariush, A., et al. 2012, *MNRAS*, 419, 1833
- Bot, C., Ysard, N., Paradis, D., et al. 2010, *A&A*, 523, A20
- Boudet, N., Mutschke, H., Nayral, C., et al. 2005, *ApJ*, 633, 272
- Carey, S., Ali, B., Berriman, B., et al. 2008, in *Spitzer Proposal ID #50398*
- Chastenet, J., Bot, C., Gordon, K. D. 2017, *A&A*, 601, A55
- Churchwell, E. B. B. L., Meade, M., R., Whitney, B. A., et al. 2009, *PASP*, 121, 213
- Compiègne, M., Verstraete, L., Jones, A., et al. 2011, *A&A*, 525, A103
- Coupeaud, A., Demyk, K., Mény, C., et al. 2011, *A&A*, 535, A124
- Dale, D. A., Aniano, G., Engelbracht, C. W., et al. 2012, *ApJ*, 745, 95
- Davies, J. I., Baes, M., Bianchi, S., et al. 2017, *PASP*, 129, 4102
- Demyk, K., Mény, C., Lu, X.-H., et al. 2017a, *A&A*, 600, A123
- Demyk, K., Mény, C., Leroux, H., et al. 2017b, *A&A*, 606, A50
- Désert, F.-X., Boulanger, F., and Puget, J.-L. 1990, *A&A*, 237, 215
- Draine, B. T., & Li, A. 2007, *ApJ*, 657, 810
- Draine, B. T., & Hensley, B. 2012, *ApJ*, 757, 103
- Dufour, R. J. 1984, *ApJ*, 287, 341
- Eden, D. J., Lie, T., Kim, K.-T., et al. 2019, *MNRAS*, 485, 2895
- Enoch, M. L., Young, K. E., & Glenn, J. 2006, *ApJ*, 638, 293
- Fernique, P., Allen M. G., Boch, T., et al. 2015, *A&A*, 578, A114
- Finkbeiner, D. P., Davis, M., & Schlegel, D. J. 1999, *ApJ*, 524, 867
- Fixsen, D. J., Cheng, E. S., Cottingham, D. A., et al. 1994, *ApJ*, 420, 457
- Fritz, J., Gentile, G., Smith, M. W. L., et al. 2012, *A&A*, 546, A34
- Galametz, M., Madden, S. C., Galliano, F., et al. 2011, *A&A*, 532, A56
- Galliano, F., Madden, S. C., Jones, A. P., et al. 2005, *A&A*, 434, 867
- Ginsburg, A., Glenn, J., Rosolowsky, E., et al. 2013, *ApJS*, 208, 14
- Gordon, K. D., Roman-Duval, J., et al. 2014, *ApJ*, 797, 85
- Hensley, B. S., & Draine, B. T. 2023, *ApJ*, 948, 55
- Hermelo, I., Relano, M., Lisenfeld, U., et al. 2016, *A&A*, 590, A5
- Holland, W. S., Bintley, D., Chapin, E. L., et al. 2013, *MNRAS*, 767, 126
- Israel, F. P., Wall, W. F., Raban, D., et al. 2010, *A&A*, 519, A67
- Izotov, Y. I., Guseva, N. G., Fricke, K. J., et al. 2014, *A&A*, 570, A97
- Jenness, T., Stevens, J. A., Archibald, E. N., et al. 2002, *MNRAS*, 336, 14
- Jones, A. P., Fanciullo, L., Köhler, M., et al. 2013, *A&A*, 558, A62
- Juvela, M., Ristorcelli, I., Montier, L., et al. 2010, *A&A*, 518, A93
- Juvela, M., Ristorcelli, I., Pelkonen, V.-M., et al. 2011, *A&A*, 527, A111
- Juvela, M., Demyk, K., Doi, Y., et al. 2015, *A&A*, 584, A94
- Katsioli, S., Xilouris, E. M., Kramer, C., et al. 2023, *A&A*, 679, A7
- Kemper, F., Vriend, W. J., & Tielens, A. G. G. M. 2004, *ApJ*, 609, 826
- Kennicutt, R. C., Calzetti, D., Aniano, G., et al. 2011, *PASP*, 123, 1347
- Kirkpatrick, A., Calzetti, D., Galametz, M., et al. 2013, *ApJ*, 778, 51
- Köhler, M., Guillet, V., & Jones, A. 2011, *A&A*, 528, A96
- Köhler, M., Stepnik, B., Jones, A., et al. 2012, *A&A*, 548, A61
- Kramer, C., Buchbender, C., Xilouris, E. M., et al. 2010, *A&A*, 518, L67
- Lequeux, J., in *IAU Symp. 108, Structure and Evolution of the Magellanic Clouds*, eds. S. van den Bergh, & K. S. de Boer (Dordrecht: Reidel), 67
- Lisenfeld, U., Israel, F. P., Stil, J. M., & Sievers, A. 2002, *A&A*, 382, 860
- Meisner, A. M., & Finkbeiner, D. P. 2015, *ApJ*, 798, 88
- Meixner, M., Galliano, D., Hony, S., et al. 2010, *A&A*, 518, L71
- Mennella, V., Brucato, J. R., Colangeli, L., et al. 1998, *ApJ*, 496, 1058
- Mény, C., Gromov, V., Boudet, N., et al. 2007, *A&A*, 468, 171
- Mizuno, D. R., Carey, S. J., Noriega-Crespo, A., et al. 2008, *PASP*, 120, 1028
- Molinari, S., Swinyard, B., Bally, J., et al. 2010, *PASP*, 122, 314
- Paradis, D., Reach, W. T., Bernard, J.-P., et al. 2009, *AJ*, 138, 196
- Paradis, D., Veneziani, M., Noriega-Crespo, A., et al. 2010, *A&A*, 520, L8
- Paradis, D., Bernard, J.-P., Mény, C., & Gromov, V. 2011, *A&A*, 534, A118
- Paradis, D., Dobashi, K., Shimoikura, T., et al. 2012a, *A&A*, 543, A103
- Paradis, D., Paladini, R., Noriega-Crespo, A., et al. 2012b, *A&A*, 537, A113
- Paradis, D., Mény, C., Noriega-Crespo, A., et al. 2014, *A&A*, 572, A37
- Paradis, D., Mény, C., Juvela, M., et al. 2019, *A&A*, 627, A15
- Paradis, D., Mény, C., Demyk, K., et al. 2023, *A&A*, 674, A141
- Pineda, J. L., Mizuno, N., Rollig, M., et al. 2012, *A&A*, 544, A84
- Planck Collaboration I. 2011, *A&A*, 536, A1
- Planck Collaboration XVII. 2011, *A&A*, 536, A17
- Planck Collaboration VIII. 2014, *A&A*, 571, A8
- Planck Collaboration IX. 2014, *A&A*, 571, A9
- Planck Collaboration XI. 2014, *A&A*, 571, A11
- Planck Collaboration XIII. 2014, *A&A*, 571, A13
- Planck Collaboration Int. XVII. 2014, *A&A*, 566, A55
- Planck Collaboration X. 2016, *A&A*, 594, A10
- Planck Collaboration Int. XXIX. 2016, *A&A*, 586, A132
- Planck Collaboration XI. 2020, *A&A*, 641, A11
- Reach, W. T., Dwek, E., Fixsen, D. J., et al. 1995, *ApJ*, 451, 188
- Rémy-Ruyer, A., Madden, S. C., Galliano, F. G., et al. 2013, *A&A*, 557, A95
- Roussel, H., Ponthieu, N., Adam, R. 2020, *Proceedings of the International Conference Observing the mm Universe with the NIKA2 Camera*
- Russel, S. C., & Dopita, M. A. 1992, *ApJ*, 384, 508
- Sadavoy, S. I., Di Francesco, J., & Johnstone, D. 2013, *ApJ*, 767, 126
- Siebenmorgen, R. 2023, *A&A*, 670, A115
- Smith, M. W. L., Eales, S. A., Gomez, H. L., et al. 2012, *ApJ*, 756, 40
- Stepnik, B., Abergel, A., Bernard, J.-P., et al. 2003, *A&A*, 398, 551
- Tabatabaei, F. S., Braine, J., Xilouris, E. M., et al. 2014, *A&A*, 561, A95
- Tibbs, C., Israel, F. P., Laureijs, R. J., et al. 2018, *MNRAS*, 477, 4968
- Turner, J. A., Dale, D. A., Adamo, A., et al. 2019, *ApJ*, 884, 112
- Ysard, N., Köhler, M., Jones, A., et al. 2015, *A&A*, 577, A110
- Ysard, N., Jones, A. P., Guillet, V., et al. 2024, *A&A*, 684, A34

Appendix A: Additional material

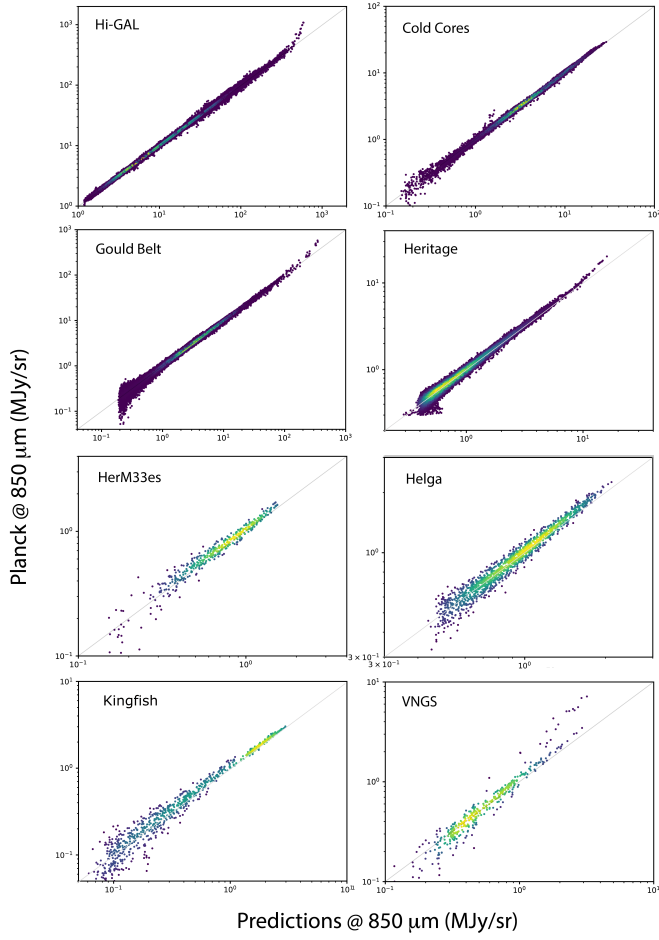


Fig. A.1. Correlation plots between *Planck* data and neural network predictions at 850 μm , for the different *Herschel* large programs.

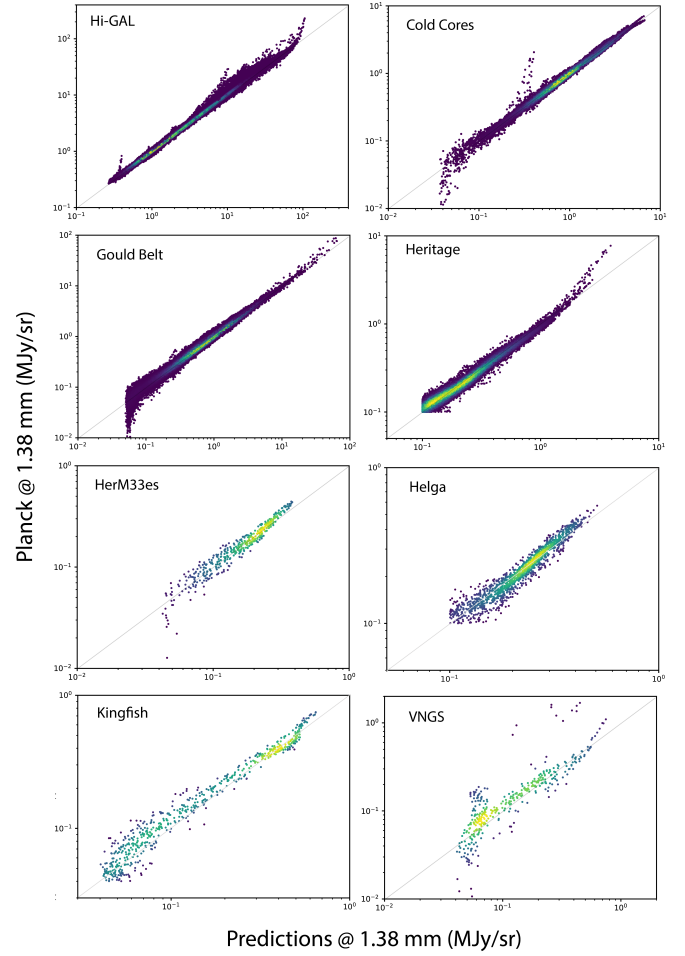


Fig. A.2. Correlation plots between *Planck* data and neural network predictions at 1.38 mm, for the different *Herschel* large programs.

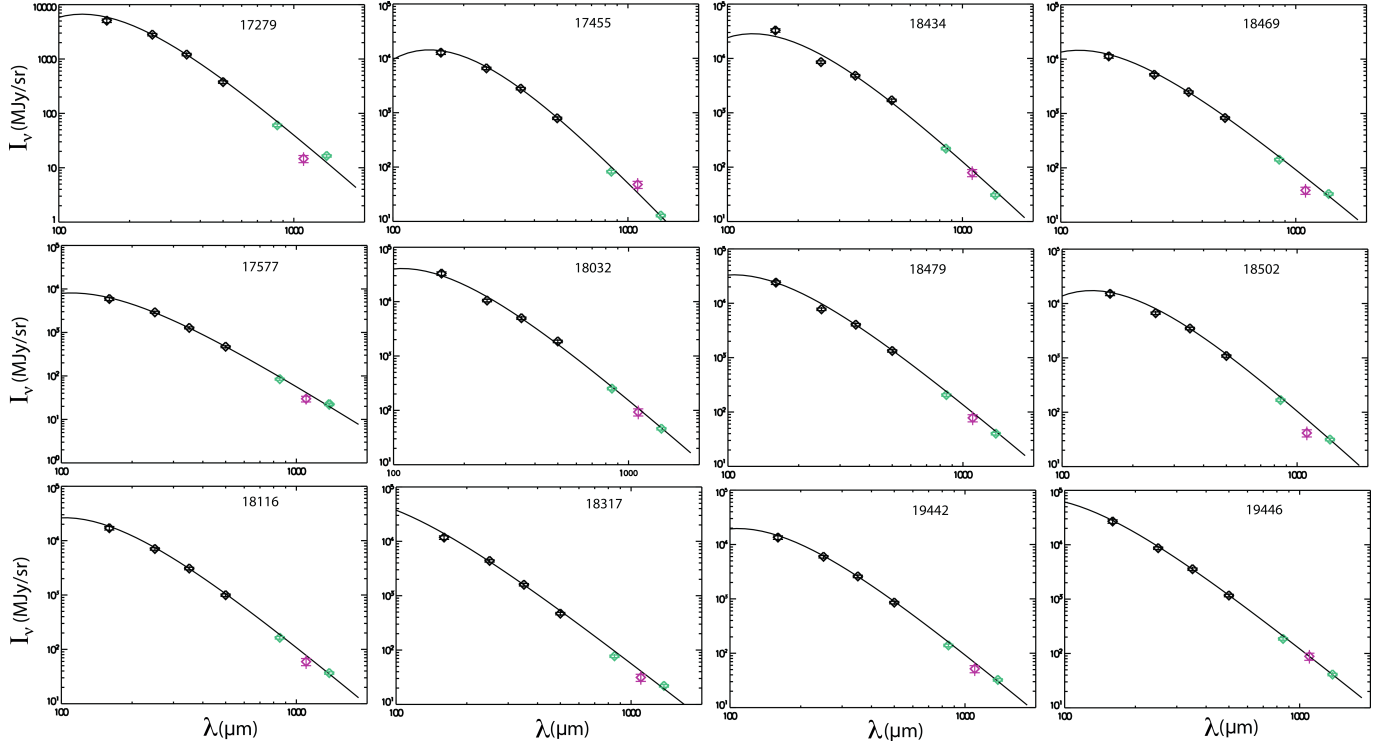


Fig. A.3. SEDs of twelve UCHII regions (coordinates given in [Paradis et al. 2014](#)), with *Herschel* data (from 160 to 500 μm) in black, Bolocam (1.1 mm) in pink, and predictions (850 and 1380 μm) in green. A modified black-body fit is shown for convenience.

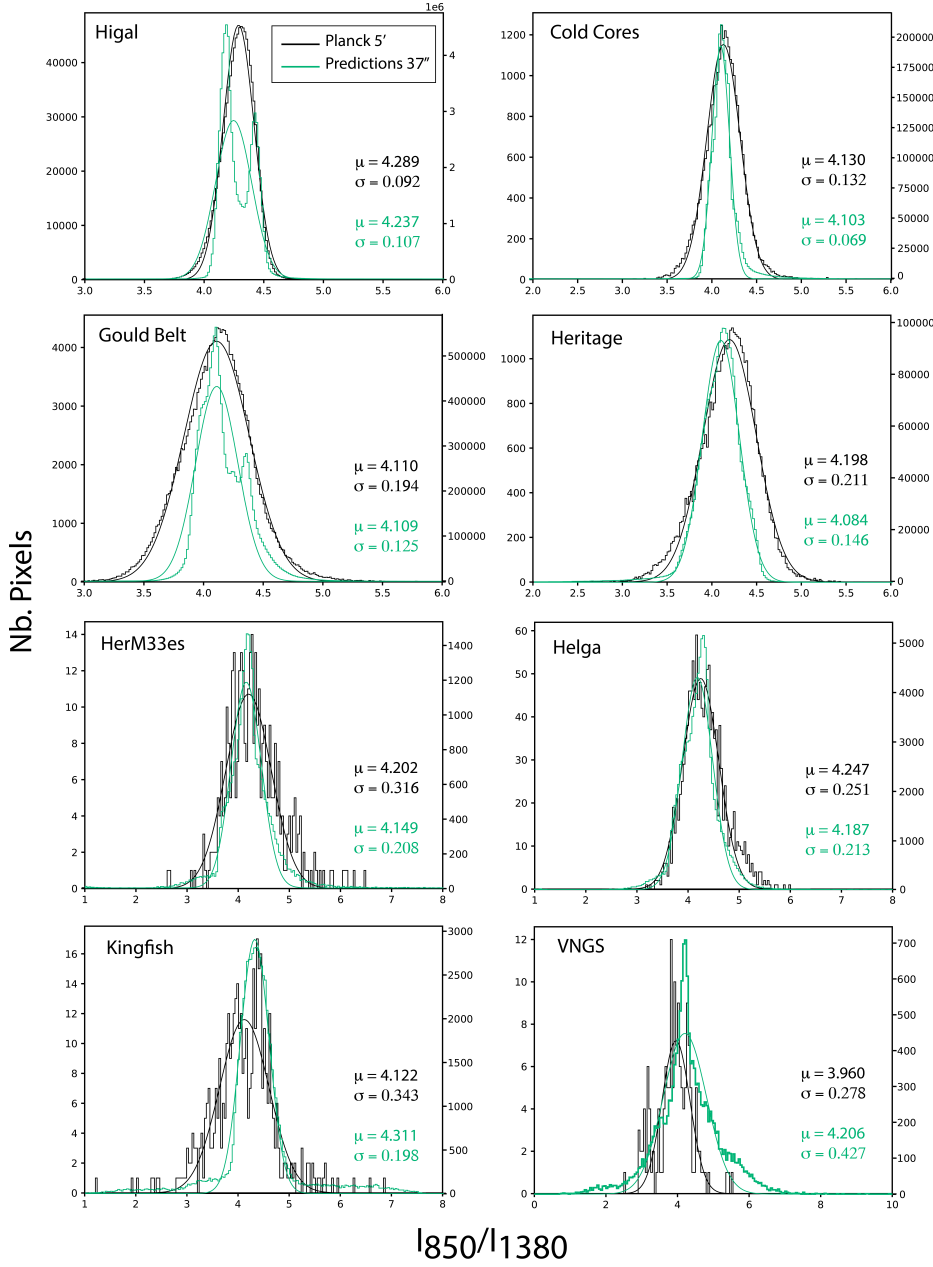


Fig. A.4. Histograms of the $I_{\nu}(850)/I_{\nu}(1380)$ ratio for each *Herschel* large program, deduced from the *Planck* data at $5'$ in black, and from the predictions at $37''$ in green. Gaussian fits are overplotted, with the central values (μ) and the standard deviations (σ) given in each panel. The left and right y axes in each panel correspond to the number of pixels for the *Planck* data and prediction histograms.